9-20-2021

FABRICATION AND COMPARATIVE STUDY OF HORIZONTAL AND VERTICAL ELECTROSPUN PROTEIN-POLYSACCHARIDE NANOFIBER BIOMATERIALS

Ashley Rivera-Galleti
Rowan University

FABRICATION AND COMPARATIVE STUDY OF HORIZONTAL AND VERTICAL ELECTROSPUN PROTEIN-POLYSACCHARIDE NANOFIBER BIOMATERIALS

by

Ashley Rivera-Galletti

A Thesis

Submitted to the
Department of Chemistry and Biochemistry
College of Science and Mathematics
In partial fulfillment of the requirement
For the degree of
Master of Science in Pharmaceutical Sciences
at
Rowan University
September 9, 2021

Thesis Chair: Xiao Hu, Ph.D.

Committee Members:
Ping Lu, Ph.D.
Kandalam Ramanujachary, Ph.D.

Acknowledgments

I would like to express my sincere gratitude to my family and research supervisor, Dr. Xiao Hu. I am thankful for the opportunity to work in his lab and gain invaluable experience and guidance throughout this research. I am grateful to the many opportunities he sought out for me to encourage my professional development and work ethics. I attended many conferences throughout the year, TA trainings, and collaborations with other universities for which I am truly grateful for what he has offered me.

As a first-generation graduate, as a woman in STEM, and as a minority, I cannot express how grateful I am to my family. Their overwhelming love, prayers, caring and sacrifices to support and cheer for my future has uplifted me during hard times. I am especially thankful to my sisters for the continuous support to complete this research work. I would truly not be here without their care and comfort if I was ever in need.

Many thanks to the members of my committee**,** Profs., Ping Lu and Chary for their guidance and help with my research-- whenever I asked, they were available to assist me, and I valued their time and contributions to my success. A special thanks to Dr. David Salas de la Cruz who provided me my very first undergraduate research experience and continuously inspired me to follow my passion for research. It was a great privilege and honor to work and study under his guidance**.** Lastly, I'd like to especially thank my fellow lab members Zhuoqi Tong and Michael Giunta, for their direct or indirect support and contributions throughout this research.

Abstract

Ashley Rivera-Galletti
FABRICATION AND COMPARATIVE STUDY OF HORIZONTAL AND VERTICAL ELECTROSPUN PROTEIN-POLYSACCHARIDE NANOFIBER BIOMATERIALS
2020-2021
Xiao Hu, Ph.D.
Master of Science in Pharmaceutical Sciences

The use of biocompatible and biodegradable composite materials for biomedical applications has attracted the attention of many researchers in the past few years. In this study, we fabricated nanofibers of silk fibroin and cellulose and its derivatives to amalgamate their unique properties into a single material. The production of these nanofibers via electrospinning is of particular interest, and whereas several studies have been done on normal nanofibers, the formation of branched nanofibers is an exciting area not currently explored. Blend solutions are formed by dissolving silk and cellulose/cellulose acetate in formic acid separately and mixing to achieve the desired ratios. Samples are electrospun in both the vertical and horizontal directions before undergoing water annealing treatment and characterization using the SEM, FTIR, TGA, and DSC. From SEM images, we find that samples spun vertically exhibit branching structures, whereas samples spun horizontally form normal nanofibers. Structural analysis shows that samples with high silk content retain the beta sheet structures and samples with high cellulose/cellulose acetate content show decreased content of random side chain groups. These results show that electrospinning can be used to fabricate branched nanofibers of silk-cellulose/cellulose acetate blends, a material that boasts attractive properties conducive to biomedical applications.

Table of Contents

Table of Contents (Continued)

Table of Contents (Continued)

Table of Contents (Continued)

List of Figures

List of Figures (Continued)

List of Tables

Table Page

Chapter 1

Introduction

1.1 Typical Proteins and Polysaccharides for Biomedical Applications

The interest in biopolymer composites have attracted many in the biomedical field encompassing drug delivery, bionanotechnology, and tissue engineering sectors. In general, a composite material can be composed of polymers, proteins, polysaccharides, or ceramics[1]. An extensive range of materials can make up composites that vary in texture, composition, and size. Biopolymers unique properties combined with metal or carbon nanoparticles can transform the material being used into an antibacterial and biocompatible product [2]. This inherent versatility offers a greater alternative to synthetic polymers alone [2].

The various biomedical applications protein-polysaccharide composites have been found in consist of wound healing, electrical devices, and nanomedicine [2]. The integration of protein–polysaccharide composites inserted into hydrogels for cartilage defects[3], electrospinning to create antimicrobial properties for wound repair [4], and generating films for use in food packaging and drug deliveries [5] have improved these processes greatly. The protein materials most commonly seen in composites include silk, keratin, soy, collagen, gelatin, and corn zein. Each protein is known to have its own unique mechanical, chemical, electrical, and optical properties, which allow for a broad range of applications [5, 6].

Naturally, proteins are synthesized in a template-directed polymerization to produce monodispersed linear polymers that form a distinct chain of monomers. A selection of broad combinations of amino acid monomers are available for synthesis in complex tissues and are linked through amide bonds where only L-amino acids are used. The primary structure of proteins is this sequence of amino acids whereas secondary, tertiary, and quaternary structures undergo the process of folding in order to assemble into its 'native' conformation [7]. Alpha helices, β-sheets, and β-turns are specific to the secondary structures in proteins where π–π interactions between aromatic amino acids and hydrogen bonding between amide bonds occur.

Protein biopolymers demonstrate the ability to respond to numerous stimuli, such as temperature, electrical, magnetic, and enzymatic stimuli in controlled settings [8]. This can greatly enhance a material specifically utilizing a proteins site of attachment at the side chains. These connections could include drugs, crosslinking agents, or pendant groups that can affect the mechanical and chemical properties of a material [9]. Protein hybrids have also been combined with other biopolymers to create multi-functional composite materials. For instance, recombinant polypeptides can be used to create materials possessing an array of functions and mechanical properties for specific tissues with the help of proteins, such as elastin and collagen [10]. Not all proteins behave similarly, for instance some proteins are limited in their cell biocompatibility or range of mechanical properties [6]. However, the majority of protein-based materials have beneficial properties in the stability of drug attachments, biodegradability, and biocompatibility.

This array of unique characteristics inherent in proteins allow them to be most favorable for use in composites [11-15].

Another biopolymer, polysaccharides offer a number of advantages over proteins for applications of material science since they are generally more stable, and usually do not denature upon heating [16]. The hydrophilic nature of polysaccharides provides another advantage in creating a polysaccharide–protein complex because of its ability to act as a stabilizing agent [17]. The sheer abundance of polysaccharides and its renewability as a natural resource makes them an inexpensive and readily available biopolymer. Some common polysaccharides are starch, cellulose, pectin, alginates, and chitosan found in plants, algae, or animals [16, 18]. The chemical makeup of polysaccharides consists of a long chain of monomeric sugars that are linked together by O-glycosidic bonds with the ability to store material, compose structural components, and act as protective materials [16, 19-21].

Polysaccharides can be depolymerized by acids, heat, specific enzymes, and high pH systems following oxidation [22]. Their hydroxyl groups can be esterified, etherified, and oxidized. While the amino groups can be acylated and deacylated and the carboxyl groups can be transformed into esters, amides, and amines [22]. Diverse in nature, polysaccharides yield materials with low, intermediate, and high molecular weights due to its polydispersity [23]. This adds to its nature of being a structurally complex molecule that may attach itself to protein or polysaccharide molecules in solution. Overall, polysaccharides offer a broad set of characteristics due to its biocompatibility, biodegradability, high chemical reactivity, and polyfunctionality [23]. Their innate

properties and variable structure yields molecular and biological advantages when used in nanomaterials and nanocomposites.

The combination of polysaccharide–protein composites for use in the biomedical field allows the formation of scaffolds, particles, films, fibers, and gels. All of this is possible due to the intermolecular interactions within their matrices [24-27]. These complex systems are formed due to the hydrophobic–hydrophobic interactions within the molecules as well as the electrostatic interactions [17]. The formation of these composites allows for the material properties of the protein to be strengthened through the blend of the polysaccharide [24]. This makes it possible to create biomaterials that take on the unique properties of each biopolymer present, such as their size [24] .

Most importantly, the fabrication of a protein–polysaccharide complex can be manipulated into exhibiting only the properties that are desired, which can enhance the mechanical properties, biodegradability, and biocompatibility of the biomaterial [28]. This may allow biopolymer composites to be fabricated on the nanometer or micrometer scales. The bio-composite nanofibers that are formed can be used for the defense or delivery of a pharmaceutical or nutrient, such as a drug or bioactive lipid [29, 30]. Overall, biopolymers with specific compositions and structures depending on their intended use can be fabricated and have a potentially limitless application in the biomedical field.

1.2 Protein Biopolymers

Protein biopolymer materials comes from the wall of plants, animals, and types of bacteria. These materials can arise from protein precursors that can be augmented by post-translational modification [31] . Protein precursors can be located at the N or C terminus of the signal peptide that is important for protein folding [32]. Much research has been applied to different kinds of proteins regarding their capabilities as a biomaterial or combination with other proteins or polysaccharides in the biomedical field. Therefore, the next section details the following protein biopolymers: Silk, keratin, soy, corn zein, collagen, and gelatin.

1.2.1 Silk

The protein silk is regarded as the toughest fiber found in nature produced by silkworms, spiders, and some insects [33-35]. Silk proteins have many favorable properties, including mechanical strength, biodegradability, and minimal immunogenicity [33, 34]. The silkworm silks are primarily comprised of fibroin and sericin proteins while spider silks consist mainly of glycine and alanine-enriched fiber proteins. The structural components of silk are made up of tightly packed beta sheet crystals known as the hydrophobic domain. Its unique structural properties come from the interspacing of hydrophobic domains by smaller hydrophilic domains [35]. While the mulberry silkworm *Bombyx Mori* spins a large amount of silk cocoons of uniform thickness, spiders can only form tiny increments of silk of varying thickness to serve a particular function. This may be why most silk proteins used

come from silkworms. In any case, silk fibers demonstrate excellent mechanical properties, high tensile strength, flexibility, and resistance to compression [33].

1.2.2 Keratin

Keratin protein is a fibrous structural protein that is found in the outer layer of skin, and serves as a structural material in hair, nails, wool, and hooves. Keratin can be classified as "soft" or "hard" where soft keratins are those that form loosely packed bundles of cytoplasmic intermediate filaments. Hard keratins are classified as intermediate filaments embedded in a matrix of cysteine-rich proteins that structure epidermal appendages [36]. Both types of keratins have similar structures in that they consist of two chains, each containing a central alpha-helical domain [37]. Keratin is extremely insoluble in water and organic solvents. However, they possess cell-binding properties that can serve as a site for cellular infiltration, attachment, and proliferation [36-38]. As a readily available protein source, they offer excellent biodegradability and biocompatibility capabilities. Due to their intrinsic capacity to self-assemble and create porous and fibrous structures, they may be selected as a biomaterial for a broad range of applications [36].

1.2.3 Soy Proteins

Soy proteins are isolated from soybeans and is mainly used for the storage of amino acids. The amino residues are linked by amide bonds into polypeptide chain monomers [39, 40]. Soy proteins have been used as a synthetic replacement for plastics. While soy has excellent environmental properties, it lacks mechanical strength and water resistance properties [41]. Three different forms of soybean products are often used in biopolymer

alternatives: Soybean whole fat (SF), soy protein concentrate (SPC), and soy protein isolate (SPI). Composite materials commonly use SPI due to its biodegradability and high strength, but SPI can be brittle and sensitive to water [42].

1.2.4 Corn Zein

Corn zein is a amphiphilic protein that accounts for about 80% of corn's protein content [43]. The dual nature of zein, with its hydrophobic and hydrophilic properties yields special characteristics such as biodegradability, biocompatibility, mechanical strength, and excellent fiber and film-forming capabilities. Zein can be divided into three classes based on solubility and molecular weight: Alpha-, beta-, and gamma-zein [43]. Zein has had recent advances as a biomaterial in the medical, pharmaceutical, and food industry fields [43, 44].

1.2.5 Collagen and Gelatin

Collagen is the main fibrous protein component in bones, cartilage, and skin [45]. It is the most abundant protein in vertebrates and invertebrates with 27 different types of collagen identified [46] . It is from collagen that the protein gelatin can be produced. By breaking cross-linkages, the partial hydrolysis of collagen or the creation of a heterogenous mixture of polypeptides from collagen produces gelatin [46, 47]. A single collagen molecule contains three alpha chains with over 1000 amino acids which can undergo post-translational modifications [48]. While collagen is insoluble, gelatin possesses qualities that make it stronger and more thermally stable [47]. The use of these biopolymers in materials have been beneficial in medical applications, such as drug delivery and implants [46, 49].

1.3 Polysaccharide Biopolymers

Polysaccharide biopolymer materials are those found abundantly in nature and have been recently exploited for their excellent structural properties to form various composites. Like proteins, polysaccharides have precursors that can be modified in cells [50]. Genes can be influenced by spatial and development changes in the nearby cells [50, 51]. After modification, precursor polysaccharides activate and possess the defined properties of their subsequent polysaccharide [52]. Because of their strong structural backbone, they have been proven to excel as biomaterials. The following polysaccharides are detailed in the next section: cellulose, chitin and chitosan, starch, and pectin.

1.3.1 Cellulose

Cellulose, the structural basis in plants, is the most abundant renewable resource on the planet [53]. An easily chemically modified polysaccharide provides many advantages as a biomaterial [54]. Cellulose has functioned as wound dressings in the form of hydrogels and scaffolds for orthopedic applications [55]. It is known that some strains of bacteria can synthesize cellulose. Its molecular structure consists of a linear homopolysaccharide with several hydroxyl groups in the thermodynamically favorable position. During synthesis, cellulose forms microfibrils with both crystalline and amorphous regions that aggregate into bigger fibrils and onto fibers.

Some common favorable properties include high tensile strength and biocompatibility. Much research explores cellulose to enhance its properties, such as phosphorylation or bacterial synthetization, which can increase its bioactivity [53, 55, 56]. Cellulose is one of the

most ubiquitous polysaccharides existing in trees, plants, and fruits, due to its important role in the cell wall of plants.

1.3.2 Chitin and Chitosan

Chitin functions as a major structural component of invertebrates, insects, and fungi [57]. The second most abundant polysaccharide found in nature, it is naturally insoluble in water. Chitin's structure is highly linear providing a highly crystalline polymer [57]. Chitosan is found in a few fungi species and is mainly produced through the deacetylation of chitin. Both biopolymers are extremely stable through hydrogen bonding owing to its high degree of crystallinity [58]. With no antigenic properties, chitin and chitosan are biocompatible as well as eco-friendly [59-61].

1.3.3 Starch

Starch is an abundant polysaccharide found in the roots, seeds, and stems of various plants and crops [62]. Composed of glucose units bound by glycosidic bonds, it is essentially comprised of the amylose and amylopectin polymer. The amylose to amylopectin ratio plays a role in the physicochemical and functional properties of starch. A few disadvantages include a low mechanical strength and high hydrophilicity, yet it demonstrates excellent biodegradability and cell seeding capabilities [63]. Starch is relatively easy to modify making it suitable to chemical enhancers to improve upon its weaker qualities [64].

1.3.4 Pectin

Pectin consists of a chain of galacturonic acid units linked by α-1,4 glycosidic bonds [65]. The galacturonic acid chain is partly esterified as methyl esters [66]. With its hydrophilic nature, it possesses many functional capabilities including its ability to increase viscosity and bind water [67]. Because of its gel-forming abilities, it has been applied in the delivery of bioactive agents. Its non-toxicity and high fiber content has made it extremely successful in the food industry [68].

Chapter 2

Fabrication And Characterization of Silk – Cellulose Acetate Nanofibers for Biomedical Applications

2.1 Introduction

Natural biopolymers are of particular interest in the fields of biomedical engineering as sustainable materials because they possess low immunogenicity, excellent biocompatibility, and outstanding mechanical properties when compared to synthetic polymers and natural tissue [69-71]. Silk, a material naturally produced by silkworms and spiders, has been used extensively in recent years in research on biomaterials. In particular, the species *Bombyx mori* produces majority of the commercially available silk products[72]. Silk possesses a multitude of properties which makes it a viable candidate for biomedical and sustainable applications, including hydrophobicity, slow degradability, biocompatibility, and mechanical properties such as strength, toughness, and flexibility [72-75]. Moreover, it is known that silk fibers possess crystalline beta-sheets, the molecular structures that give silk its phenomenal strength [76].

As a derivative of cellulose, an abundant biopolymer found in plants, cellulose acetate (CA) is viable as a sustainable biomaterial. Properties of CA that make it conducive for biomedical applications include biocompatibility, hydrophilicity, water absorption and retention abilities, and water transport abilities [77-79]. However, CA also has poor resistance, low breaking stress, and low breaking strain, properties that would make it unsuitable for biomedical applications [78-80]. Nonetheless, applications of

electrospun CA in biomedical sciences include regenerative medicine, drug delivery, and cell culture[79]. Additionally, a variety of studies on blends of CA with other polymers have been done to investigate the properties of the blend polymers [78, 80-85]. Moreover, there is evidence that CA can improve mechanical properties when blended with other polymers [85]. Due to the hydrophilicity of CA, it is an unsuitable material for certain applications such as wound healing and tissue engineering. Since silk is hydrophobic, blending silk and CA could produce a sustainable material that inherits the best properties of silk and CA, making it suitable for certain biomedical or green applications. For example, a material that possesses the mechanical strength, beta sheets and hydrophobicity from silk and the water absorption and water retention capabilities from CA, could be an excellent candidate for scaffolding in tissue engineering.

A viable and versatile method of fabricating one-dimensional ultrathin natural polymer fibers is by electrospinning, a process whereby liquid polymer solutions turn into nanofibers upon interactions with an applied electric field [86] . Different materials can be blended in a solution homogeneously when electrospinning, producing nanofibers with controlled ratios of different components [87] . Combinations of different ratios of materials may result in novel discoveries regarding the physico-chemical and biological properties of the electrospun nanofibers. In addition, nanofibers can be either regular or branched, where branched nanofibers usually have increased surface area to volume ratio, enhanced fiber entanglement and improved scaffold porosity[88-91]. Several studies have shown that branched nanofibers perform extremely well for their applications due to their unique properties [88-91][20-23]. Furthermore, whereas some study had to utilize additional

processing to generate branched nanofibers [88][20], many studies showed branched or regular nanofibers can be generated directly from altering spinning parameters and polymer solutions when electrospinning in different directions [88-91].

The two standard ways of electrospinning are spinning in the vertical direction, where the electric field is parallel to the gravitational field; and spinning in the horizontal direction, where the electric field is perpendicular to the gravitational field. Previous studies on the impact of horizontal and vertical spinning on the morphology of the nanofibers have shown that gravity difference between the different spinning setups can affect the structures of the resulting nanofibers [92-94]. Nanofibers that differ in properties such as porosity and fiber diameter have potential for varying applications. If the spinning direction adds another tunable layer to the spinning process, this holds great value in areas where nanofiber properties must be controlled. In our study, we discovered that dominated branched nanofibers of silk and CA blends were formed when spinning in the vertical direction as opposed to the horizontal direction.

A proposed mechanism for the formation of branched nanofibers during electrospinning involves the instabilities in the polymer fluid jet caused by the combination of surface tension and electric stresses [95] . In addition, the dynamics due to the orientations of the electric and gravitational fields in vertical spinning likely also contributes to the formation of branched nanofibers. The unique properties of branched nanofibers combined with the properties of silk and CA make branched nanofibers of silk

and CA blends more suitable for certain biomedical applications such as wound dressing and scaffolding in tissue engineering when compared to regular nanofibers.

While one study has investigated the electrospinning of silk and CA nanofibers from trifluoroacetic acid solution [96], the vertical/horizontal electrospinning of branched or regular nanofibers of silk-CA blends from a mild (formic acid-$CaCl_2$) solution for biomedical applications remains an unknown area. In this study, the goal is to compare the nanofibers from electrospinning varying blends of silk and cellulose acetate both in the vertical and horizontal spinning directions. Results showed that the vertical spinning direction forms dominated branched nanofibers, whereas the horizontal spinning direction produces regular nanofibers with different structural, thermal, and mechanical properties. Gaining insight into how the morphology of silk-CA nanofibers can be controlled provides a way to further explore the various applications of these sustainable materials.

2.2 Materials and Methods

2.2.1 Preparation of Materials

Bombyx mori silk cocoons, purchased from Treenway Silks (Lakewood, CO, USA), were first degummed to remove sericin from the fibers. The degumming procedure included boiling 10 grams of silk cocoons in a 3L solution dissolved with 6.36 grams of $NaHCO_3$ (Sigma-Aldrich, St. Louis, MO, USA) for 30 minutes, which includes 15 minutes of stirring, before rinsing for 20 minutes in 1.5L DI water baths a total of three times. In order to remove excess moisture on their surface, the fibers were then air

dried overnight before being placed into a vacuum oven for a 24-hour period. Formic acid (ACS Grade 98%), anhydrous calcium chloride, and cellulose acetate powder were purchased from EMD Millipore Corporation (Burlington, MA, USA), AMRESCO Inc. (Solon, OH, USA), and Sigma Aldrich Co., LTD (St. Louis, MO, USA), respectively. All chemicals were used as purchased.

2.2.2 Polysaccharide-Protein Composite Fibers

For this study, a total of seven weight ratios of cellulose acetate to silk were fabricated as follows: pure CA (CA100), 90:10 (CA90S10), 75:25 (CA75S25), 50:50 (CA50S50), 25:75 (CA25S75), 10:90 (CA10S90), and pure silk (Silk100). The CA and the silk were dissolved separately in a solution of formic acid with 4% (w/v) $CaCl_2$ (FA) and blended to make each ratio. When preparing the CA solution, a glass vial was used to keep the solution constantly mixing with a magnetic stir bar on an unheated hot plate. The CA solution was mixed until total dissolution occurred no less than 2 hours. Silk dissolved quickly into the solvent and then it was immediately mixed with the CA solution. Finally, a Benchmark BV1000 BenchMixer vortex mixer was used to vortex the solution for one minute at 3200 rpm before being added to an Air-Tite Luer-Lock syringe. After mixing, the solution sample was immediately loaded onto the auto pump and the electrospinning procedure commenced.

Both the vertical and horizontal directions for electrospinning were set up using a syringe automatic pump (Harvard Apparatus Model 22, Holliston, MA). In both setups, the applied voltage was 15 kV, and the flow rate was controlled at 10 µl/min. In addition,

the humidity was controlled by using a custom-made polycarbonate box and dehumidifier unit. The observed humidity fell in the range of 20-35% relative humidity for both setups. In the vertical setup, a 20×20 cm metal plate covered with aluminum foil was placed approximately 30 cm below the tip of the needle to collect the electrospun samples. In the horizontal setup, the aluminum covered parallel plates were placed approximately 10 cm in front of the needle tip to collect the samples.

All samples were spun in both directions, and each sample was spun for around 3~5 hours to ensure the collection of the electrospun nanofibers. The nanofiber mesh was then dried in a vacuum oven for 24 hours to remove formic acid residues. The collected samples were named as-spun (AS) samples. As-spun samples were also annealed in deionized (DI) water for 30 mins to remove $CaCl_2$ residues and then dried in a vacuum oven for another 24 hours. These samples are named water-annealed (WA) samples.

2.2.3 Scanning Electron Microscopy (SEM)

An FEI VolumeScope™ SEM (Hillsboro, Oregon, USA) was utilized for the assessment of the morphology of the silk-CA nanofibers. The SEM directs four beam currents at the sample to show the details of the blended fibers on a microscopic level. To prepare for the SEM, samples were placed on SEM holders, held in place with carbon tape, and coated with a layer of gold in the Denton Vacuum Desk sputtering machine for 10-15 seconds. Afterward, the samples were placed into the SEM for imaging. Pictures were then taken at scale bars of 50 µm, 25 µm, and 5 µm.

2.2.4 Fourier Transform Infrared Spectroscopy (FTIR)

A Bruker Tensor 27 Fourier Transform Infrared Spectrometer (Billerica, MA, USA) was used to conduct the FTIR analysis of the silk-CA fibers. The spectrometer had additions of a deuterated triglycine sulfate (DTGS) detector as well as a multiple reflection, horizontal MIRacle ATR attachment, which used a germanium crystal from Pike Tech. (Madison, WI, USA). 64 background and sample scans were taken at a 2 cm^{-1} resolution in the range of 4000 to 400 cm^{-1}. Multiple areas were used in triplicate to sample and to ensure a homogeneous distribution in the fibers. Between each sample, ethanol was used to clean the germanium crystal; it was then allowed to air dry. The OPUS software was used to isolate and focus on specific regions of the spectra of each sample.

2.2.5 Differential Scanning Calorimetry (DSC)

DSC analysis of the silk-CA nanofiber samples were conducted using a Q100 DSC (TA Instruments, New Castle, DE, USA) with a refrigerated cooling system and a nitrogen purge gas that flowed at 50 mL/min through the sample chamber. Prior to use, heat flow and temperature were calibrated using an indium crystal and heat capacity was calibrated using sapphire standards. Aluminum pans were used to hold approximately 6 mg of the samples before being pressed closed. For the temperature-modulated differential scanning calorimetry (TMDSC), the heating rate was set at 2 °C/min, with a modulation period of 60 seconds, and the temperature amplitude was set at 0.318 °C, ranging from -40°C to 400°C. To check whether steady state was achieved, plots of the

Lissajous figures of modulated heat flow vs. Modulated temperature were made, providing data regarding heat flow and the reversal of heat capacity versus temperature.

2.2.6 Thermal Gravimetric Analysis (TGA)

A Q600 SDT instrument (TA Instruments, Wilmington, DE, USA) with a small ceramic pan and a precision balance inside the furnace was utilized for the TGA analysis of the nanofibers. The internal temperature was equilibrated to 30 ℃ before being increased by 10 ℃ per minute to 600 ℃, and the purge gas used was nitrogen with a rate of 100 mL/min. To determine the thermal stability of the samples, percent mass measurements were taken vs. temperatures.

2.2.7 Mechanical Testing

Mechanical properties of dense nanofiber mesh were characterized using a Shimadzu mechanical tester (Japan). To prepare the samples for stress-strain tensile testing, the nanofiber mesh was cut into rectangular shape. Strips of nanofiber mats were carefully cut out to minimize the manipulation of samples prior to tensile testing. The measured length of the specimen is 30 mm, and the width of the sample is 10 mm. The average thickness of the electrospun fiber mesh is around 0.1mm. The size of each sample is recorded individually. Each end of the sample was securely fixed onto double sided tapes, and the tapes were loaded between the test clamps. The mounted sample was aligned in the vertical direction. The method used for load normalization of tested data was the specimen mass equation. This was used to calculate the stress and Young's modulus of the electrospun fiber mesh. A 100 N load cell was used with a strain rate of 1

mm/min. After the tensile test, the specimen was recovered and weighted for the stress (σ) calculation according to Equation (1).

$$\sigma_{eq} = \rho_m \frac{F}{m} L \quad (1)$$

2.3 Results and Discussion

2.3.1 Morphology Analysis

The SEM images for the vertically electrospun samples of silk-CA blends, shown in Figure 2.1a, reveal detailed morphological and structural patterns in the various blends silk and CA. The structures of the nanofibers in the blends were significantly different from the structures in both the pure silk and the pure CA nanofibers. In the pure silk sample (Silk100), it can be seen that the nanofibers do not have uniform fiber diameters. The images of the Silk-CA composite samples (90S-10CA, 75S-25CA, 50S-50CA, 25S-75CA,10S-90CA) show that the nanofibers from those two blends have relatively uniform fiber diameters. In addition, an interesting phenomenon observed in these blends is the branching of individual fibers, which can be clearly seen at the 25 μm and 5 μm scales of the silk dominated fibers (Silk100, 90S-10CA or 75S-25CA).

For CA dominated samples (10S-90CA or 25S-75CA), the fibers tend to have more loops and coils. However, silk-dominated fibers (90S-10CA or 75S-25CA) are mostly straight, indicating that these samples have higher mechanical strength. This may be due to the higher mechanical properties of silk β-sheet crystals compared with CA molecules. As the silk content decreases, the rigidity of the fibers also decreases, and coil

structures appear in the fiber network. In addition, the fiber diameters also decrease as silk content decreases. Moreover, the porosity of these nanofibers also decreases as the CA content increases, except for the CA100 sample, in which regular nanofibers did not form using this electrospinning method.

Figure 2.1

SEM Images of Silk-Cellulose Acetate Nanofibers

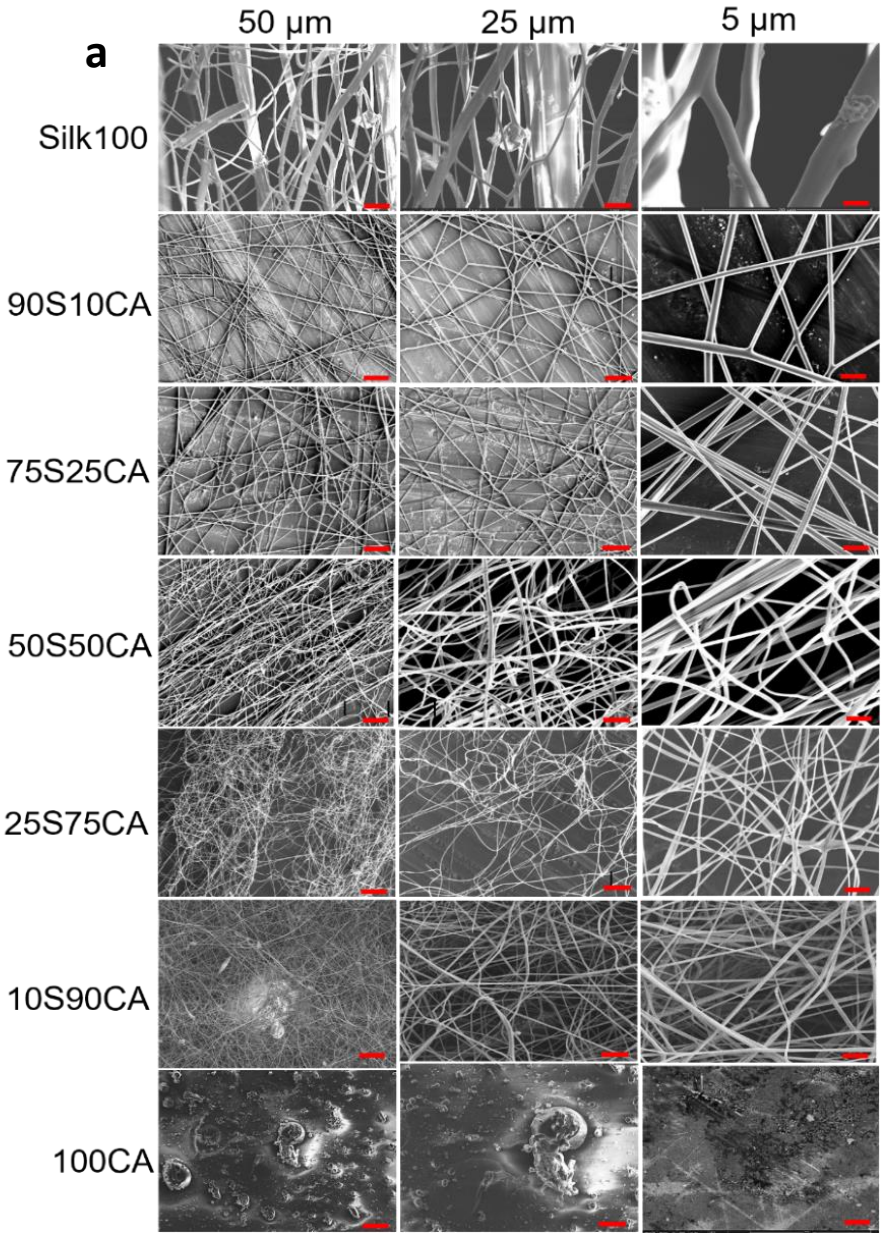

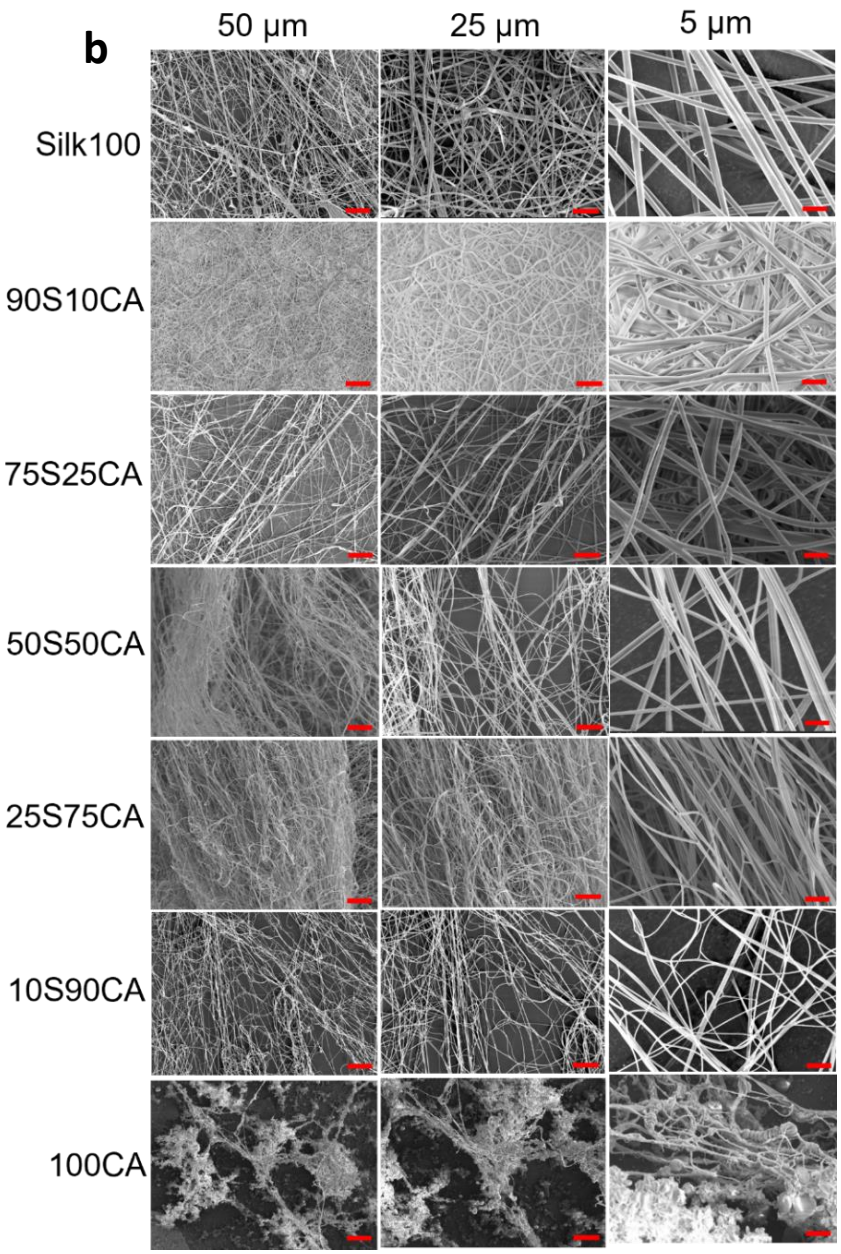

Note. SEM images of (a) vertically spun and (b) horizontally spun silk-cellulose acetate nanofibers at different ratios.

The SEM images for the horizontally electrospun samples of silk-CA blends are shown in Figure 2.1b. Compared to the vertically electrospun samples, the horizontally

spun samples show many of the same characteristics with a few differences. The biggest difference in the horizontally spun samples is that those samples did not form any obvious branching, whereas branching was clearly observed in the vertically spun samples. Two major trends can also be observed for these nanofibers. The first trend is that as the silk content decreases, the average fiber diameter also decreases. For example, at the 5 μm scale, the Silk100 fibers had larger average diameters than the fibers in the S10-90CA sample. The second observable trend is that as the silk content decreases, the fibers also become more elastic. The high rigidity in the samples with high silk content is likely due to the β-sheets present in the silk, and the low rigidity in the samples with low silk content is likely due to the higher CA content, which is known to be weaker than silk.

2.3.2 Structural Characterization

Structural analysis was conducted on samples of the silk-CA blends electrospun both vertically and horizontally as well as for both before and after water annealing. The water annealing process was conducted by annealing the samples in DI water for 30 minutes to understand the structural transitions of the fiber materials. The spectra used for understanding the secondary structures of the silk proteins as well as the CA structures are the peaks in the Amide I (1600~1700 cm^{-1}), Amide II (1500~1600 cm^{-1}), and C-O-C stretching (950~1150 cm^{-1}) regions.

In the vertical as spun (AS) samples, all samples with silk proteins exhibited a peak in the Amide I region at around 1640 cm^{-1} (Figure 2.2a). This shows that the

predominant secondary protein structures in these silk-CA nanofibers were random coils. After water annealing (WA), this peak showed a shift in the Amide I region from 1640 cm^{-1} to ~1620 cm^{-1}, indicating that the predominant secondary structures in the water-annealed silk-CA nanofibers were crystalline beta-sheets (Figure 2.2c). In addition, for both the AS and the WA samples with silk proteins, peaks centered at around 1540-1515 cm^{-1} were evident in the IR spectra. These peaks fall under the Amide II region and are typically associated with loose-chain side groups within the protein matrix (Figure 2.2a, 2.2c)

In addition, the spectra for both the AS and WA samples show that the presence of CA can alter the structures of the nanofibers significantly. For both samples with CA molecules, a peak centered at around ~1720 cm^{-1} started appearing and the peak centered at around 1540-1515 cm^{-1} started disappearing when and after the sample exceeded 25% CA (see spectra in both Figure 2.2a and Figure 2.2c). The 1720 cm^{-1} peak can be associated with the stretching of the carbon - oxygen double bond in the acetyl group of CA. This agrees with the observed pattern in that the peaks centered at around 1720 cm^{-1} diminishes in intensity as the percentage of silk in the sample is increased.

Additionally, in both the AS and WA samples, the peak centered at around 1520 cm^{-1} also disappears as more CA is present in the samples. The disappearance of this peak indicates that as CA is introduced into the nanofibers, the loose chain side groups gradually disappear (Figure 2.2a and 2.2c). The spectra in Figure 2.2b and Figure 2.2d confirm the CA content in the samples since the peaks corresponding to C-O-C stretching

in the CA backbone centered at around 1020 cm^{-1} and 1050 cm^{-1}, respectively, increased in intensity as the percentage of CA in the samples increased.

Figure 2.2

FTIR Absorbance Spectra for Vertical and Horizontal Electrospun Silk-Cellulose Acetate Nanofibers

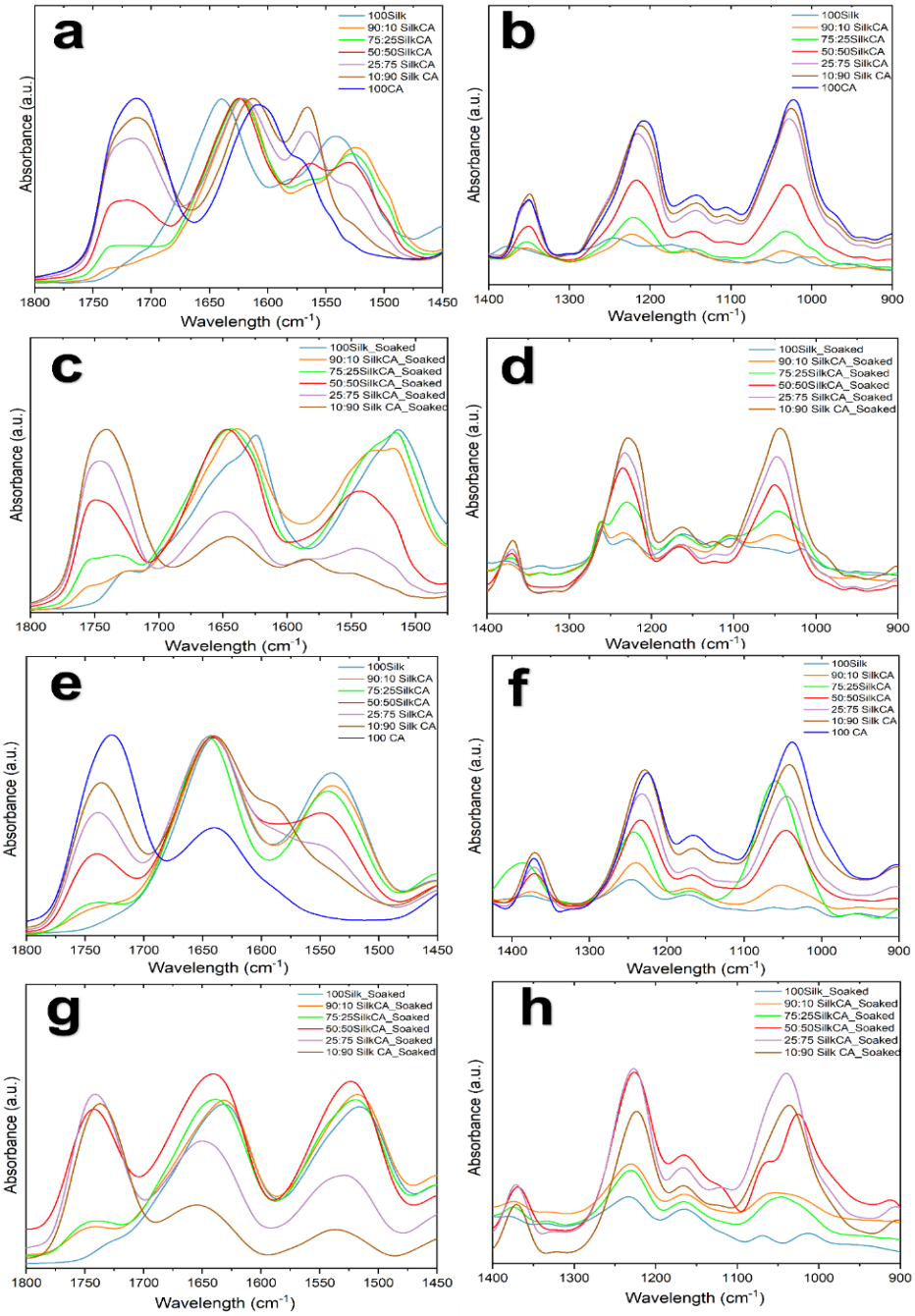

Note. (a) Infrared spectrum of Amide I and II Regions of vertically electrospun silk-CA blends before water annealing. (b) shows the (AS) cellulose acetate regions. (c) Infrared spectrum of vertically electrospun silk-CA blends after water annealing amide I and II regions. (d) shows the after water annealing cellulose acetate regions. (e) Horizontally electrospun Infrared spectrum Amide I and II regions, before water annealing. (f) shows the associated cellulose acetate regions. (g) Infrared spectrum of horizontally electrospun silk-CA blends after water annealing. (h) shows (WA) cellulose acetate regions.

Moreover, in the spectra for the WA samples (Figure 2.2c), the shifted peak at ~1620 cm^{-1} also started to disappear and slightly shifted to the left as the CA concentration increased. This is most noticeable when and after the CA content exceeded 75% (Figure 2.2c). This demonstrates that the content of beta-sheet crystals gradually disappears as the silk content is decreased. This agrees with existing research since beta-sheet crystals are present in silk protein but not in CA.

A very interesting phenomenon is observed in the AS samples at the peak centered at ~1565 cm^{-1} (Figure 2.2a). For both the pure silk and pure CA samples, no peaks are observed there. However, peaks start appearing as the two samples are mixed, with the intensity directly proportional to the CA content in the samples. This likely indicates that the silk protein and CA molecules are interacting to form certain structures, which rely more on the availability of CA to form. Since this peak disappears after water annealing (Figure 2.2c), these structures are not permanent, and can easily be destroyed upon interaction with water.

Similar to the vertically spun samples, all the as spun (AS) samples with silk proteins exhibited a peak in the Amide I region at around 1640 cm^{-1} (Figure 2.2e), confirming the predominant secondary protein structures as random coils. After water annealing (WA), this peak showed a shift in the Amide I region from 1640 cm^{-1} to 1620 cm^{-1}, indicating that the predominant secondary structures in the water-annealed silk-CA nanofibers were crystalline beta-sheets (Figure 2.2e). In addition, for both the AS and the WA samples with silk proteins, peaks centered at around 1520 cm^{-1} were evident in the IR spectra. These peaks fall under the Amide II region and are typically associated with loose-chain side groups within the protein matrix (Figures 2.2e, 2.2g).

In addition, the spectra for both the AS and WA samples show that the presence of CA can alter the structures of the nanofibers significantly. Specifically, noticeable effects are observed at the peaks centered around 1720 cm^{-1} and 1520 cm^{-1} (see spectra in both Figure 2.2e and Figure 2.2g). The 1720 cm^{-1} peak can be associated with the stretching of the C-O double bonds in the acetyl groups, and the 1520 cm^{-1} peaks are associated with loose chain side groups, as mentioned earlier. The general trend observed is that the peaks centered at around 1720 cm^{-1} diminish in intensity as the percentage of silk in the sample is increased. Additionally, the peak centered at around 1520 cm^{-1} also disappears as more CA is present in the samples. The disappearance of this peak suggests that as CA is introduced into the nanofibers, the loose chain side groups gradually disappear.

The spectra in Figure 2.2f and Figure 2.2h confirm the CA content in the samples since the peaks corresponding to C-O-C stretching in the CA backbone centered between 1020 cm^{-1} and 1050 cm^{-1}, increased in intensity as the percentage of CA in the samples increased. Moreover, in the spectra for the WA samples, the shifted peak at 1620 cm^{-1} also started to shift towards 1640 cm^{-1} as the CA concentration increased (Figure 2.2g). This demonstrates that the content of beta-sheet crystals gradually disappears as the silk content is decreased. This agrees with existing research since the presence of beta-sheet crystals is attributed to silk protein.

Interestingly, the peaks centered at around 1565 cm^{-1} observed in the vertically spun samples are not observed in the horizontally spun samples. This suggests that vertical electrospinning is capable of catalyzing interactions between silk and CA leading to the formation of temporary structures, whereas horizontal electrospinning may not have those capabilities.

2.3.3 Thermal Analysis by DSC

Temperature-modulated DSC (TMDSC) was conducted to gain further insight into the thermal properties of the silk-CA nanofibers, and the results for the vertical electrospun nanofibers after water annealing are shown in Figure 2.3a and 2.3b. The first peaks, observed at around 60-70 degrees Celsius, correspond to the solvent evaporation temperature (T_s). For this study, the solvent was formic acid, and at the T_s, the remnants of the excess formic acid and water in the samples were vaporized. The shifted peak for the 50silk-50CA sample at 111.23 ˚C indicates that the solvent retention abilities for that

sample were better than the other samples. Surprisingly, whilst CA is known for its water retention capabilities, the samples containing greater than 50 percent of CA had a lower T_s than the 50silk-50CA sample. Apart from the 50silk-50CA sample, the T_s steadily decreases as CA content diminishes with just 10% CA having the lowest value of 57 ˚C.

Although not obvious from the heat flow plot (Figure 2.3a), the peaks that correspond to the glass transition temperature (T_g) can be seen between 180 and 200 degrees Celsius. The T_g can be seen clearly between 180-200 degrees Celsius in the reversed heat capacity plot (Figure 2.3b). Moreover, there is only one defined T_g for every sample, indicating that the polymers are fully miscible. The third major peak which lies between 260 and 300 degrees Celsius indicates the degradation temperature (T_d), which is consistent with the degradation temperature observed from the TGA results.

All the samples, including the blended samples, show only one peak at that region. This indicates that the polymer degrades once and fully degrades, which shows that the fiber interactions within the blended samples are excellent. Previous film studies have shown that the T_g of silk-CA films are in the range of 120 - 200 degrees Celsius. In this study, we find that the T_g of silk-CA nanofibers are in the range of 180 - 210 degrees Celsius, indicating that silk-CA nanofibers possess better thermal stability than silk-CA films.

Figure 2.3

DSC Thermograms of Vertical and Horizontal Electrospun Silk-Cellulose Acetate Nanofibers

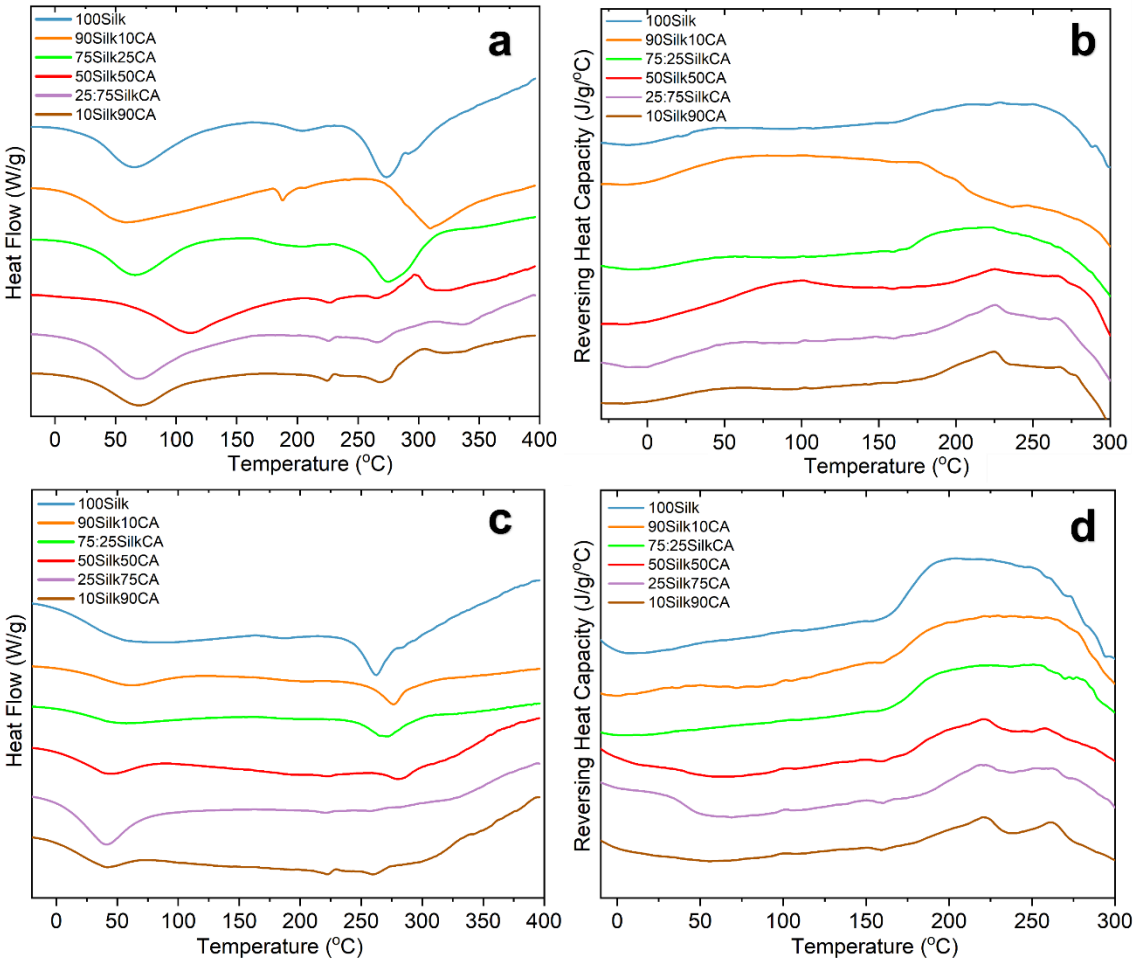

Note. TMDSC plots of vertically electrospun silk-CA composites after water annealing. Heat flow is shown in (a) and reversing heat capacity is shown in (b). Plots of horizontally electrospun silk-CA composites after water annealing. Heat flow is shown in (c) and reversing heat capacity is shown in (d).

The TMDSC plots of the water annealed silk-CA nanofibers spun horizontally are shown in Figure 2.3c and 2.3d. From the heat flow plot (Figure 2.3c), the T_s can be observed between 40-60 degrees Celsius. Surprisingly, the sample with 10 percent CA possesses greater solvent retention capabilities than the samples with higher CA content. Although the T_g is unclear from the heat flow plot, the heat capacity plot (Figure 2.3d) clearly shows that the T_g lies between 180 and 200 degrees Celsius, similar to the results from the vertically spun samples. The T_d is found at a temperature range between 260 and 280 degrees Celsius. Similar to the vertically spun samples, the horizontally spun samples also have only one degradation peak, indicating that the horizontally spun composites are also fully miscible and that the interactions between silk and CA are excellent. Thermogravimetric analysis (TGA) was used to gather additional information about the thermal stability of the silk-CA composite fibers.

2.3.4 Thermal Gravimetric Analysis (TGA)

The TGA results for the vertically electrospun samples are shown in Figure 2.4. The plots in Figure 2.4a show the mass percent over time as temperature is increased and the plots in Figure2.4b show the derivative of the mass percent as temperature is increased. In Figure 2.4b, peaks corresponding to the T_s can be observed at around 44-54 degrees Celsius. This is due to the removal of the moisture and solvent in the samples, previously absorbed by the hygroscopic nature of Silk and CA biomaterials. The TG plot also shows a slight decrease in mass (9.71%) for the 10S-90CA sample at this junction. This agrees with the knowledge that CA possesses excellent water retention abilities

since the solvent evaporation temperature was observed much later for the 10S-90CA sample.

The degradation temperature of these samples can be seen in both Figure 2.4a and Figure 2.4b, although Figure 2.4b shows the major degradation peak $_{much}$ clearer. In general, all samples had an increasing degradation peak as the percentage of silk increased. Specifically, the 10 percent silk sample had the lowest value, and the pure silk sample had the highest value. This makes sense since CA is mechanically weaker than silk, and so the presence of CA in the polymer blends should make the polymer easier to degrade. Surprisingly, the 75 percent silk sample had a T_d similar to that of the 10 percent silk sample seen in Table 2.1. From Figure 2.4a, it can be clearly seen that after degradation, the samples with high silk content retained the most amount of its original mass and the samples with low silk content retained the least amount of its original mass at 600 ˚C.

From Figure 2.4b, the major degradation peaks are shown. The pure silk fiber understandably has the highest max degradation temperature value of 342˚C.

Surprisingly, the mass retention for the pure silk sample lied in between the mass retention for the blended samples, indicating that pure silk is not as strong as composite samples and pure CA is not as weak as composite samples. This indicates that in low amounts, the addition of CA does indeed increase the strength of silk-CA nanofibers.

Figure 2.4

TGA Thermograms of Vertical Electrospun Silk-Cellulose Acetate Nanofibers

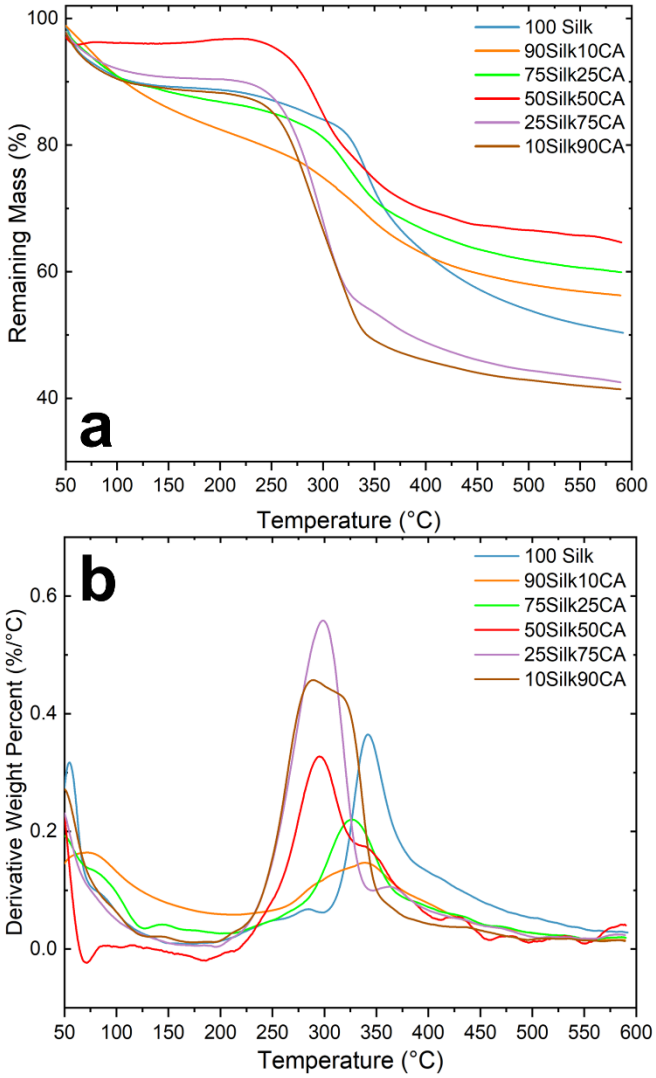

Note. TGA plots of vertically electrospun silk-CA composites after water annealing. Mass percent is shown in (a), and the first derivative of weight is shown in (b).

The TGA results for the horizontally spun samples are shown in Figure 2.5, with mass percent shown in Figure 2.5a and first derivative shown in Figure 2.5b. The T_s can be observed at around 40 degrees Celsius for all the samples in Figure 2.5b. Additionally, the major degradation peak corresponding to the temperature range of 280 - 360 degrees Celsius are seen Figure 2.5b. Interestingly, the major degradation peaks increase as the content of silk decreases, which seems counterintuitive given that pure silk is known to be incredibly strong. However, looking at the mass percent plots in Figure 2.5a, the samples with higher silk content retained more of its mass post degradation than samples with higher CA content. Surprisingly, the pure silk sample retained less mass than the samples with 10 and 25 percent CA content. This trend is also observed in the vertical spun samples, indicating that the presence of small amounts of CA can improve the thermal stability of these samples.

Moreover, all the vertically spun samples retained more mass post degradation at 600 °C than their respective polymer ratios spun horizontally as seen in Table 2.1 and Table 2.2. For example, the vertically spun S90CA10 sample retained ~60 percent of its original mass, whereas the horizontally spun S90CA10 sample only retained ~40 percent of its original mass. This shows that vertically spun samples exhibit greater thermal stability than horizontally spun samples, likely due to the branching observed, as discussed previously. The thermal analysis data for the vertically spun samples are summarized in Table 2.1 and the data for the horizontally spun samples are summarized in Table 2.2.

Figure 2.5

TGA Thermograms of Horizontal Electrospun Silk-Cellulose Acetate Nanofibers

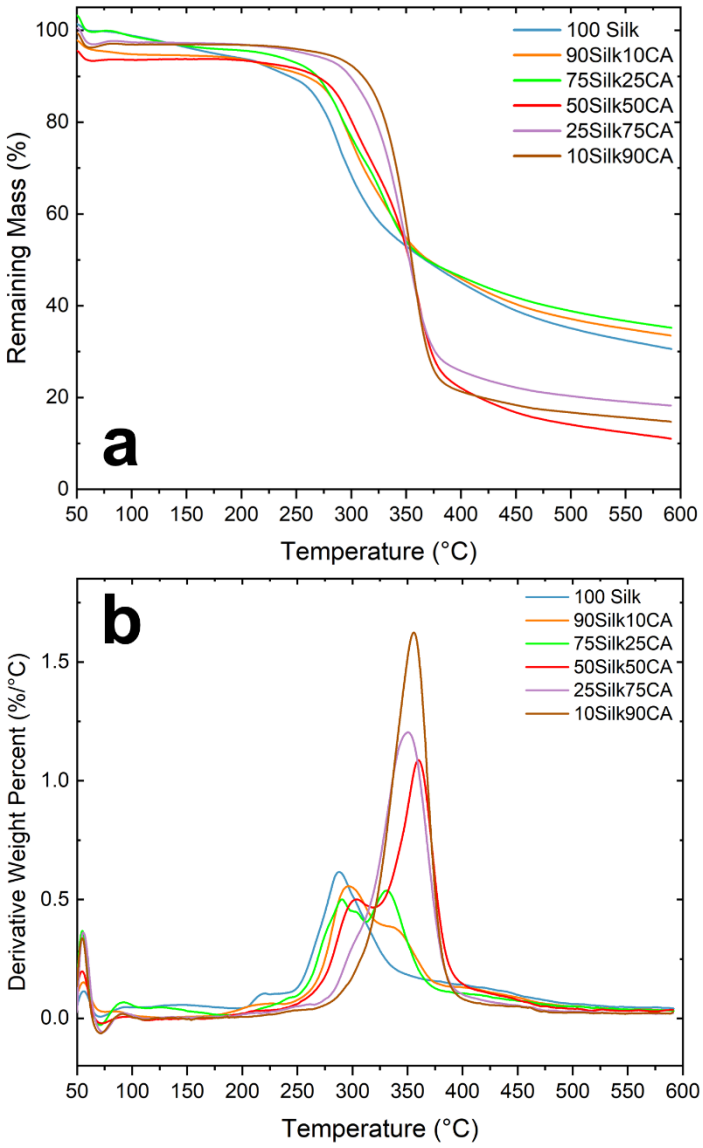

Note. TGA plots of horizontally electrospun silk-CA composites after water annealing. Mass percent is shown in (a), and the first derivative of weight is shown in (b).

Table 2.1

Thermal Analysis Data of Vertically Spun Silk-CA Nanofibers

Sample	T_g (°C)	Solvent Release T_s (°C)	T_d (°C)	T_{Onset} (°C)	Bound Solvent Content (%)	T_{end} (°C)	Remaining Mass at 600°C (%)
Silk100	184.38	63.67	273.03 - 291.29	300.79	12.28	400.30	50.34
S90CA10	187.74	57.93	309.62	286.76	13.12	376.26	56.26
S75CA25	200.28	65.46	274.60	283.81	12.26	350.53	59.91
S50CA50	201.34	109.22	263.41	211.67	3.74	388.24	64.62
S25CA75	208.74	66.96	263.84	247.27	9.51	385.27	42.53
S10CA90	206.35	68.38	268.12	240.63	9.71	341.09	41.42

Note. All numbers have an error bar within ±5%. The first three columns (T_g, T_s and T_d) were determined by TMDSC analysis, T_g, T_s and T_d represent the glass transition temperature, bound solvent release peak temperature, and degradation peak temperature of different silk-CA nanofibers, respectively. The remaining columns (T_{Onset}), Bound Solvent Content, (T_{end}), and Remaining Mass at 600°C were determined by TG analysis where T_{Onset}, T_{end} represents the initial and final decomposition temperatures, respectively.

Table 2.2

Thermal Analysis Data of Horizontally Spun Silk-CA Nanofibers

Sample	T_g (°C)	Solvent Release T_s (°C)	T_d (°C)	T_{Onset} (°C)	Bound Solvent Content, (%)	T_{end} (°C)	Remaining Mass at 600°C (%)
Silk100	172.24	46.44	261.68	248.46	2.49	341.13	30.16
S90CA10	174.76	57.40	276.20	250.04	3.18	362.09	34.19
S75CA25	175.94	47.41	265.21	250.88	4.43	358.79	34.08
S50CA50	185.51	37.91	274.66	270.91	2.78	379.82	11.45
S25CA75	198.38	39.37	-	275.55	3.07	375.55	18.09
S10CA90	199.64	33.23	-	292.56	2.6	379.14	14.79

Note. All numbers have an error bar within ±5%. The first three columns (T_g, T_s and T_d) were determined by TMDSC analysis, T_g, T_s and T_d represent the glass transition temperature, bound solvent release peak temperature, and degradation peak temperature of different silk-CA nanofibers, respectively. The remaining columns (T_{Onset}), Bound Solvent Content, (T_{end}), and Remaining Mass at 600°C were determined by TG analysis where T_{Onset}, T_{end} represents the initial and final decomposition temperatures, respectively.

2.3.5 Mechanical Testing Analysis

Tensile testing was conducted to analyze the mechanical strength of the different nanofiber composites, spun in both the vertical and horizontal directions. Figure 2.6 shows the stress-strain curves for the vertically spun samples and Figure 2.7 shows the curves for the horizontally spun samples. For both the vertically and the horizontally spun samples, the general trend for the Young's modulus observed is as follows, from samples with the lowest modulus to samples with the highest modulus: S10CA90, S25CA75, S50CA50, S75CA25, S90CA10, S100CA0. Notable exceptions include the S90CA10 sample spun in the vertical direction, the S90CA10 sample spun in the horizontal direction, and the pure silk sample spun in the horizontal direction. In the samples spun vertically, the ultimate tensile strength (UTS) decreases as the amount of silk in the sample decreases, with the exception of the 90S10CA sample. This makes sense since the beta sheet content in silk gives silk its strength, and with less silk in the sample, less beta sheet crystals will be present and hence the strength will be decreased. Surprisingly, in the horizontally spun samples the pure silk sample had a lower UTS than the 90S10CA and 75S25CA samples. This indicates that trace amounts of CA may actually provide these horizontally spun nanofibers greater strength.

However, adding too much CA will significantly decrease the strength of the samples, as seen in Table 2.4. In the vertically spun samples, no clear trend was observed for the elongation. However, in the horizontally spun samples, the samples with higher CA content possessed decreased elongation when compared to the samples with higher

silk content. This is surprising since the SEM images showed that the samples with higher CA content had more elastic fibers. One plausible explanation is that the strength of the samples with high silk content causes the sample to withstand more stretching than the samples with higher CA content, which are mechanically weaker.

Figure 2.6

Stress-Strain Curve Plot of Horizontal Silk-Cellulose Acetate Nanofibers

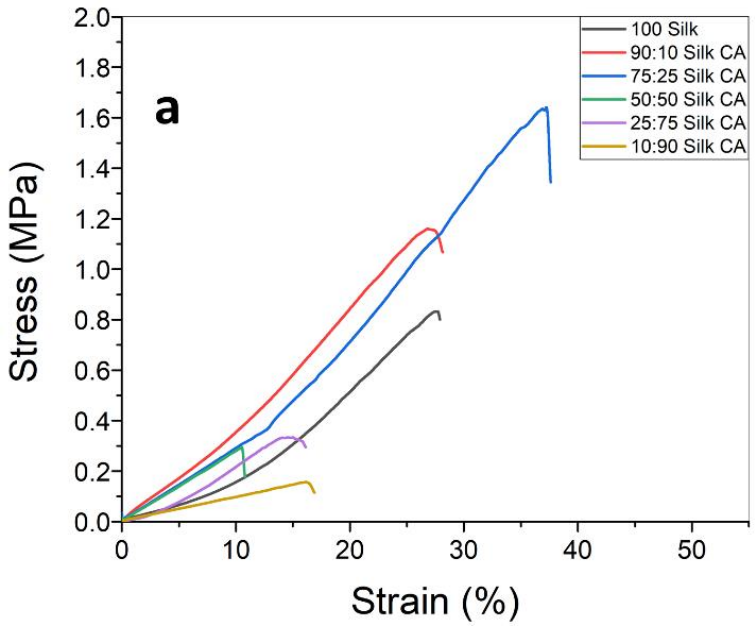

Note. Tensile test results of horizontally spun Silk-CA composite nanofibers.

Table 2.3

Mechanical Properties of Horizontally Spun Silk-CA Nanofibers

Sample	Elastic Modulus (MPa)	Ultimate Tensile Strength (MPa)	Elongation (%)
Silk100	2.6	0.8	28
S90CA10	4.25	1.07	28
S75CA25	3.6	1.35	37
S50CA50	2.8	0.18	11
S25CA75	2.4	0.29	16
S10CA90	1	0.12	17

Figure 2.7

Stress-Strain Curve Plot of Vertical Silk-Cellulose Acetate Nanofibers

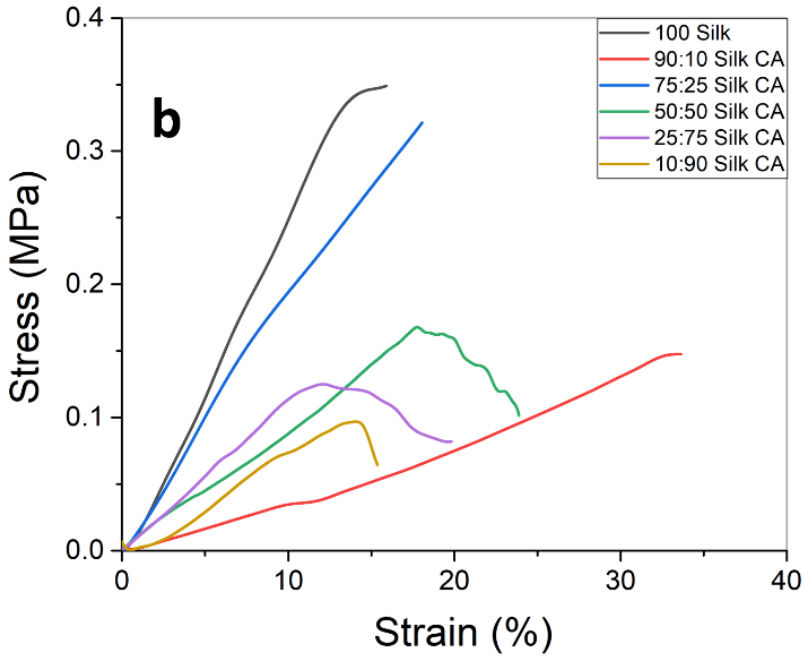

Note. Tensile test results for vertically spun Silk-CA composite nanofibers.

Table 2.4

Mechanical Properties of Vertically Spun Silk-CA Nanofibers

Sample	Elastic Modulus (MPa)	Ultimate Tensile Strength (MPa)	Elongation (%)
Silk100	2.5	0.35	16
S90CA10	0.4	0.148	34
S75CA25	2	0.325	18
S50CA50	0.938	0.1	24
S25CA75	1.2	0.08	20
S10CA90	0.7	0.065	15.5

2.3.6 Mechanism of Interaction

Based on the results discussed above, a proposed mechanism for the nanofiber formation is outlined in Figure 2.8. After silk and cellulose acetate are dissolved in solution, cellulose acetate units arrange themselves within the larger structure of silk. The CA units interact with the beta sheets of silk via hydrogen bonding between the double bonded oxygens in the acetyl groups of CA and the amine groups of the silk beta sheets. Differences due to the orientation of the gravitational field and the electric field likely contributes to the formation of branching in the nanofibers. Interactions within the polymer jet in the vertical direction due to the parallel nature of the gravitational field and the electric field is a likely source of the branching observed in the SEM images. These

same interactions may have been hindered by the fact that the gravitational field and electric field are perpendicular to each other when spinning horizontally. Other researchers have also proposed mechanisms that focus heavily on the electrostatic interactions inside the polymer jet [95].

Figure 2.8

Mechanism of Interaction

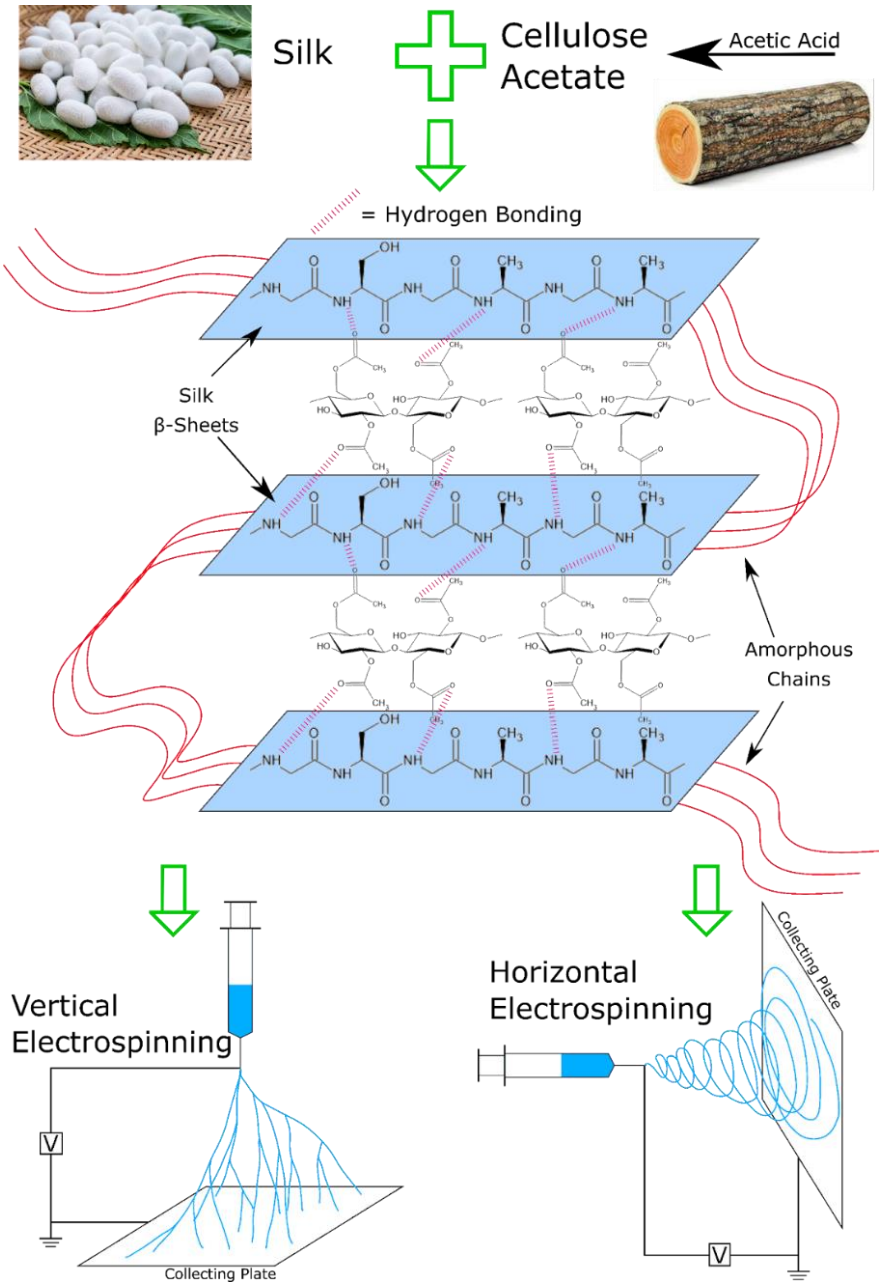

Note. Schematic describing the fabrication mechanism for horizontal and vertical electrospinning.

2.4 Conclusions

In summary, blends of silk and cellulose acetate were electrospun in both the horizontal and vertical directions to fabricate nanofibers. The physical properties and topographical features of these nanofibers were characterized with FTIR and SEM, and the thermal properties were characterized with TGA and DSC. Electrospinning in the vertical direction produced branched nanofibers, whereas horizontal electrospinning produced normal nanofibers. From the structural analysis of all composite samples, it can be concluded that the addition of CA preserves the beta sheets usually found in silk, showing that these polymer blends can indeed retain the strength of pure silk when mixed with CA. From the analysis of the silk-CA composite nanofibers thermal data, DSC and TGA results reveal that the vertically spun samples exhibit greater thermal stability than horizontally spun samples.

The results from mechanical testing show that the horizontally spun samples elastic moduli are no lesser than two times that of vertically spun samples. This confirms horizontally spun samples have greater stiffness and resistance to bend or stretch. Since the elastic modulus for polymers rely on the intermolecular forces, this reveals that the horizontally spun samples have higher intermolecular forces. Normally an organic polymer carbon chain with many branching chains detracts from the surface area of the molecule, limiting the opportunities for intermolecular forces. In this case, the more branches on the hydrocarbon, the less surface area they have so the forces are weaker. Given the structural nature and assembly of the vertically spun nanofibers, this could

potentially be the case. However, molecular branching also affects chain entanglement or the ability of chains to slide past one another, in turn affecting physical properties including thermal stability.

While long chain branches may increase polymer strength, toughness, and the glass transition temperature due to an increase in the number of entanglements per chain, a random and short chain length between branches, on the other hand, may reduce polymer strength causing a disruption to the chains ability to interact with each other or crystallize. Given the results, nanofibers with different properties can be produced with varying content of silk and CA and of differing spinning directions. Depending on the specific needs of certain applications, different ratio blends can be chosen as materials for those applications, including but not limited to tissue scaffolding and wound dressing.

Chapter 3

Electrospun Silk-Cellulose Formate Nanofibers with Tunable Properties

3.1 Introduction

Electrospinning is a technique using polymer solutions and an electric field to produce nanofibers [86, 87]. Electrospinning can produce nanofibers with straight, branched, and coiled morphologies. There is growing interest in controlling fiber morphology due to a desire for materials with high surface area to volume ratios and varying degrees of porosity. Many factors influence fiber morphology such as the inherent properties of the polymer and solvent, concentration of the polymer solution, solution viscosity, flowrate, applied voltage, distance from the needle tip to grounded collector, and relative humidity of the air [97]. One novel way to select for different morphological properties is by altering the electrospinning direction [98-100]. The two standard electrospinning setups are horizontal and vertical [101].

In a horizontal setup, the needle is placed parallel to the ground while the collector is placed perpendicular to the ground. In a vertical setup, the needle is placed perpendicular to the ground and the collector is placed parallel to the ground. Pal et al. demonstrated that branched nanofibers can be fabricated through vertical electrospinning after a short duration of solution stirring (5 minutes) [98]. While short periods of mixing yielded branched nanofibers, long periods of mixing (12 hours) yielded compact, conventional nanofibers. Suresh et al. fabricated branched nanofibers in both the horizontal and vertical directions; however, at a certain blend ratio, their vertically spun

branched fibers were heterogeneous (micro and nanoscale) and had a significant increase in mean porosity and fiber diameter, leading to increased cell viability [99] . Khatri et al. found that spinning corn-zein fibers in the horizontal direction gave straight nanofibers, and spinning in the vertical direction gave coiled-fibers [100]. These findings indicate that while numerous factors affect nanofiber properties, the electrospinning setup clearly plays a significant role as well.

Cellulose is an abundant and renewable polysaccharide that is primarily sourced from plant cell walls. It is a linear molecule composed of repeating glucose monomers, granting it hydroxyl side groups along its backbone. The molecular properties of cellulose grant it many desirable properties such as great tensile strength and biocompatibility [102]. However, the disadvantages of cellulose include high mechanical stiffness and poor solubility in many solvents [17]. Reactions with these hydroxyl side groups allow cellulose to be derivatized into many forms. One derivative - cellulose formate – can be easily produced via esterification between the hydroxyl groups of cellulose and formic acid at room temperature, substituting formyl groups along the cellulose backbone [103-106] . Up to this point, little research has been conducted on cellulose formate due to its instability to heat. Despite this instability, cellulose formate, unlike pure cellulose, is readily soluble in organic solvents such as formic acid, DMSO, and pyridine [104]. Cellulose formate's enhanced solubility and instability to high temperatures make it extremely interesting as an intermediary to produce materials with tailored properties. For instance, upon boiling in hot water, pure cellulose can be regenerated from cellulose formate [104]. Cellulose formate can also be converted into other

cellulose derivatives such as cellulose sulfate upon reaction with SO¬3/DMF [103]. Cellulose sulfate has been cited as having numerous biomedical-related applications such as terrific anticoagulant activity, biocompatibility, biological activity, and chemical stability [107]. In addition, cellulose formate was recently used to react with silver compounds to make cellulose formate-Ag composite materials with excellent antimicrobial properties [105].

One of the most versatile natural polymers is silk. While silk is produced by many organisms, the most studied variety of silk to date is produced by the Mulberry species Bombyx mori [108, 109] . Silk has many unique properties due its ability to possess five different types of molecular organizations including coiled coil, extended beta sheet, cross-beta sheet, collagen-like triple helix, and polyglycine II [110, 111]. Silk is a protein mainly composed of beta sheet crystals due to the many large hydrophobic domains in its structure, and altering the beta sheet content varies its mechanical, thermal, and chemical properties [35]. Silk is a desirable protein due to its impressive flexibility, high tensile strength, good biocompatibility, slow biodegradability, controllable structure, and ability to self-assemble [112, 113].

Protein-polysaccharide composite materials can be fabricated to strengthen the properties of each individual polymer. Proteins and polysaccharides strengthen each other through hydrophobic-hydrophobic interactions and electrostatic interactions [17]. The blending of the polysaccharide helps to stabilize the protein-polysaccharide matrix due to its hydrophilicity and ability to control the aqueous phase rheology [24] . Polymer blending

is advantageous because various blend ratios allow for a tunable material with varying properties; polymer blending can yield enhanced biodegradability, biocompatibility, and mechanical properties. Research has shown that upon blending, silk helps to enhance cellulose's poor tensile modulus, and the overall composite is granted greater thermal stability [114]. However, to date, there has been no published research citing the properties of silk-cellulose formate materials.

In this study, blend electrospinning is used to fabricate silk-cellulose formate nanofibers of various ratios in both the horizontal and vertical directions. Various analyses were done on the fibers to determine if their morphological, structural, and thermal properties can be controlled by altering the blend ratios and electrospinning setup. The nanofibers were characterized using scanning electron microscopy (SEM), Fourier-transform infrared spectroscopy (FTIR), differential scanning calorimetry (DSC), and thermogravimetric analysis (TGA). By gaining insight into how to control the morphology of these silk-cellulose formate nanofibers, various applications could be pursued as biomaterials as well as eco-friendly, sustainable materials.

3.2 Materials and Methods

3.2.1 Preparation of Materials

Bombyx Mori silk cocoons were purchased from Treenway Silks (Lakewood, CO, USA). In order to use the silk, treatment is needed to degum the fibers from the sticky sericin coating. The silk cocoons are degummed by way of boiling in a solution of 0.02 M Na2CO3 (Sigma-Aldrich, St. Louis, MO, USA). The silk was then soaked in

deionized water three consecutive times to ensure the removal of the sericin coating and to extract the fibers. The silk fibers were then air dried overnight and placed in a vacuum at room temperature for a 24 hr. period to extract any remaining moisture held within the fibers. The cotton linter cellulose, Whatman Filter Paper Grade 597 Optima (VWR, Radnor, PA, USA) is made from >98% alpha cellulose. Formic Acid (ACS Grade 98%) was purchased from EMD Millipore Corporation (Burlington, MA, USA). All the listed chemicals were used as purchased.

3.2.2 Polysaccharide-Protein Composite Fibers

The air-dried silk fibroin (SF) fiber was placed in a glass vial with a 4% $CaCl_2$-formic acid solvent to form a 0.10g SF/mL solution. To fully dissolve the SF, the solution was shaken on a vortex BenchMixer at 3,200 rpm for 10 minutes. The Whatman filter paper was also mixed in a glass vial with a 4% calcium chloride-formic acid solvent. The solution was constantly stirred using a magnetic stir bar over a hotplate for 48 hours at 40 °C to allow for the complete reaction of cellulose with formic acid, forming cellulose formate (CF). This procedure yielded a 0.10g CF/mL solution. The SF and CF solutions were then combined to a given ratio using a volumetric pipette and clean vial. The solution was shaken using a vortex mixer for 10 minutes to get them completely mixed. A total of 7 weight ratios were selected: 100% Silk (100 Silk), 90% Silk-10% Cellulose Formate (90:10 SC), 75% Silk-25% Cellulose Formate (75:25 SC), 50% Silk-50% Cellulose Formate (50:50 SC), 25% Silk-75% Cellulose Formate (25:75 SC), 10% Silk-90% Cellulose Formate (10:90 SC), and 100% Cellulose Formate (100 CF).

3.2.3 Scanning Electron Microscopy (SEM)

Scanning Electron Microscopy (SEM) was used to measure the surface morphology of fiber and film samples using a LEO 1530 VP SEM at an EHT of 10 kV. Prior to imaging, samples were sputter coated with gold for 15 s.

3.2.4 Fourier Transform Infrared Spectroscopy (FTIR)

FTIR analysis of the silk-cellulose formate fibers was overseen by using a Bruker Tensor 27 Fourier Transform Infrared Spectrometer (Billerica, MA, USA). The FTIR spectrometer had an addition of a triglycine sulfate detector and a multiple reflection, horizontal MIRacle ATR attachment (using a Ge crystal, from Pike Tech. (Madison, WI, USA)). A total of 64 background scans and 64 sample scans were taken from the 4000 cm-1 to 400 cm-1 range at a resolution 2 cm-1 for each sample measurement. Samples were taken from multiple spots and sides in triplicate to ensure a homogeneous distribution in the fibers. Ethanol was used to clean the Ge crystal between samples. Spectra from each sample were isolated with focus on the selected regions using the Opus data processing software to process the samples.

3.2.5 Differential Scanning Calorimetry (DSC)

Approximately 3-5 mg of nanofiber samples were enclosed in an aluminum pan and pressed closed to prepare for DSC analysis. A Q100 DSC (TA Instruments, New Castle, DE, USA) equipped with a refrigerated cooling system was used for the analysis. 50 mL/min of nitrogen purge gas was pumped through the sample chamber. To calibrate

the instrument prior to use, an indium crystal was used for heat flow and temperature, while aluminum and sapphire standards were used for the heat capacity. Temperature-modulated differential scanning calorimetry (TMDSC) measurements were performed at a heating rate of at 2 °C/min with a modulation period of 60s and temperature amplitude of 0.318K, from -40°C to 400°C. To verify the establishment of a steady state, the Lissajous figures of modulated heat flow vs. modulated temperature were also plotted. This will give data regarding the heat flow and reversing heat capacity versus the temperature. The fourteen different samples produced were analyzed using this test.

3.2.6 Thermal Gravimetric Analysis (TGA)

Thermogravimetric analysis (TGA) of silk-cellulose formate nanofibers was performed with a TA Instruments Q600 SDT instrument (Wilmington, DE, USA). The TGA had a precision balance with a small plastic pan inside of the furnace of which its temperature was controlled to raise the temperature from equilibration point of 30℃ to 600℃ at a consistent rate of 10℃/min. Nitrogen purge gas was used at a rate of 100 mL/min. The mass of the samples was measured over time with regards to changing temperatures with the purpose of measuring the thermal stability of the samples.

3.2.7 Horizontal & Vertical Electrospinning

Horizontal and vertical electrospinning were performed for each weight ratio, yielding twelve unique samples. Both setups, as well as a simple procedural outline, are shown in Figure 1. Both horizontal and vertical electrospinning were performed with a 15 kV applied voltage at room temperature. A syringe pump (Harvard Apparatus Model 22,

Holliston, MA) maintained the solution flow rate at 10 µl/min for both setups. The humidity was observed and ranged from RH value of 20-35%. All electrospun samples were collected between two parallel metal plates lined with aluminum foil. For the horizontal setup, the collector was placed 10 cm from the needle tip; for the vertical setup, the collector was placed 20 cm from the needle tip.

Figure 3.1

Silk-Cellulose Nanofiber Synthesis

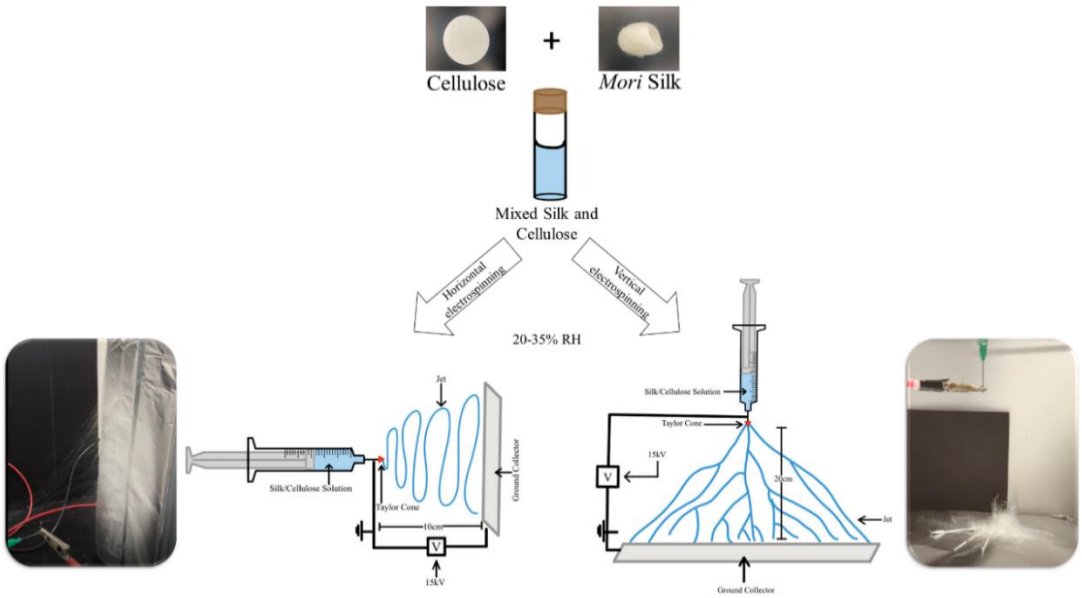

Note. Procedure for the creation of silk-cellulose formate fibers made using a $CaCl_2$-formic acid solvent and electrospinning in both the horizontal and vertical directions.

3.3 Results and Discussion

3.3.1 Structural Characterization

FTIR analysis was performed to investigate the conformations of the polymer chains as well as the molecular interactions in the various blend ratios. FTIR spectra of the blend ratios for the unsoaked, electrospun fibers are depicted in Figure 3.2. The horizontally spun samples in Fig. 3.2a depicts the silk-dominant Amide I and Amide II region of the spectrum and Fig. 3.2b depicts the cellulose-dominant 1400-900 cm^{-1} region of the spectrum. In Fig. 3.2a, nanofiber samples with silk show a distinct peak at around 1640 cm^{-1} indicative of the amide I region of silk. With increasing cellulose formate content, this amide I peak shifts from 1640 cm^{-1} (100 Silk) to 1644 cm^{-1} (10:90 SC). This wavenumber shift with increasing cellulose formate indicates the formation of a more alpha helical and random coil structure due to interactions between the two polymers. All the samples containing silk also show a characteristic peak at around 1530-1550 cm^{-1} representative of the Amide II region of silk. There is a significant wavenumber shift in the amide II region with increasing cellulose formate from 1530 cm^{-1} (100 Silk) to 1550 cm^{-1} (10:90 SC). This indicates alterations occurring in the side chain group of silk when blended with cellulose formate. Fig.3.2a also shows a distinct peak at 1715 cm^{-1} that increases in intensity with increasing cellulose formate. This peak represents the H-bonded C=O bonds from its formyl groups [106]. Fig. 3.2b shows characteristic peaks of cellulose formate at 1055 cm^{-1} and 1157 cm^{-1}, representing the C-O-C stretching vibrations of the molecule.

Figure 3.2c and 3.2d depicts the FTIR data for the vertically spun nanofibers. In Figure 3.2c, the silk dominant region of the FTIR plot show the vertically spun fibers have the same characteristic peaks and peak shifts as those seen horizontally for the amide I region, amide II region, and C=O stretch of the formyl group. For the amide I region, there is a similar peak shift from 1641 cm^{-1} (100 Silk) to 1645 cm^{-1} (10:90 SC) with increasing cellulose formate. There is also a peak shift in the amide II region from 1536 cm^{-1} (100 Silk) to 1550 cm^{-1} (10:90 SC). Just as the horizontal fibers, there is a peak 1715 cm^{-1} representing an H-bonded C=O stretch.

Figure 3.2d shows the C-O-C stretching vibration in cellulose formate at 1055 cm^{-1} and 1157 cm^{-1} that increases in intensity with increasing cellulose formate content. While similar to the horizontal data, the vertical FTIR data shows a few differences. For instance, for the vertical silk dominant samples in Figure 3.2c, there is a less significant peak shift in the amide I and amide II regions. While there are notable shifts horizontally when comparing the 90:10 SC sample to the 100 Silk sample, these shifts are not as evident in the vertical samples. These peak shifts are also less pronounced vertically when comparing the 75:25 SC sample to the 100 Silk sample. This indicates that the vertical, silk-dominant samples more closely retain the properties of pure silk.

Figure 3.2

FTIR Absorbance Spectra of Silk-CF Nanofibers

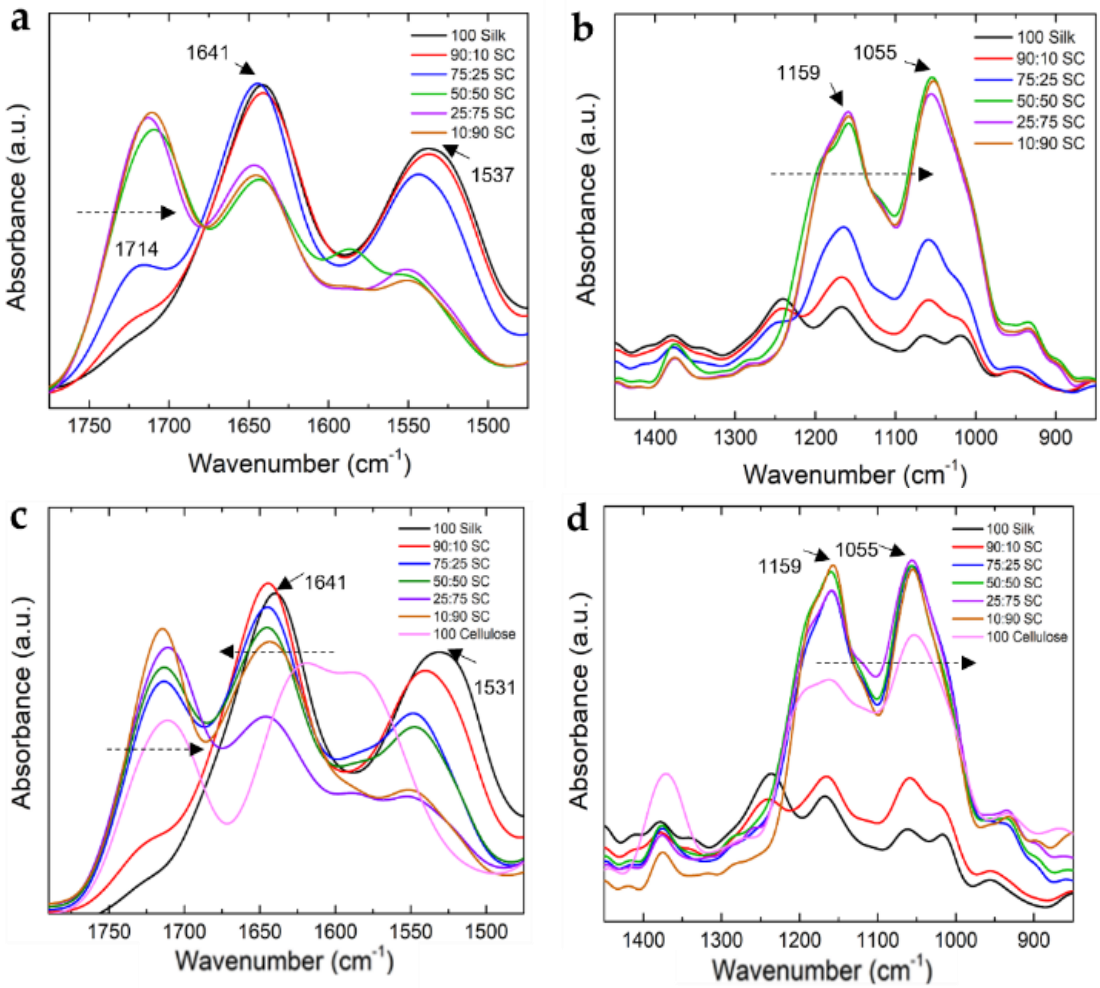

Note. FTIR of horizontally spun silk-cellulose formate samples showing the (a) silk-dominant region 1800-1475cm^{-1} and (b) cellulose formate dominant region of 1450-850 cm^{-1}. FTIR of vertically spun silk-cellulose formate samples (c) silk-dominant region 1800-1475cm^{-1} and (d) cellulose formate dominant region of 1400-850 cm^{-1}.

3.3.2 Thermal Analysis by DSC

Thermal analysis was first performed using temperature modulated differential scanning calorimetry (TM-DSC). This was performed to understand the thermal properties of the silk-cellulose formate nanofibers, as shown in Figure 3.3 and Figure 3.4. The TMDSC data for the horizontally spun fibers can be seen in Figure 3.3. Figure 3.3a depicts that each sample shows an initial peak at ~ 75 °C representing overlap of the solvent evaporation temperature (T_S), and the glass transition temperature (T_g). The data then shows a two-step degradation process for all the composite samples, with the first peak representing cellulose formate and the second representing pure silk [115].

Figure 3.3

DSC Thermograms of Horizontal Silk-CF Nanofibers

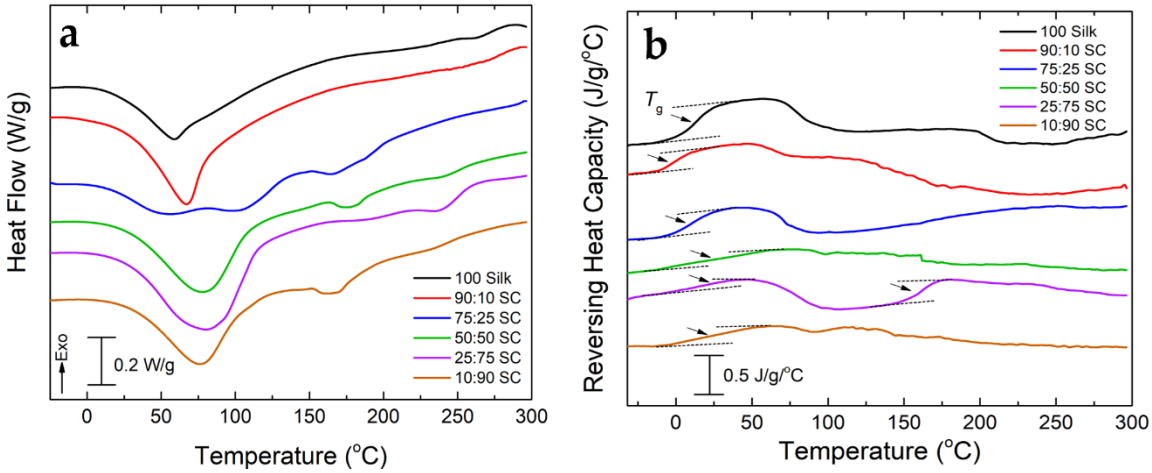

Note. TMDSC plots of horizontally electrospun silk-CF composites after water annealing. Heat flow is shown in (a) and reversing heat capacity is shown in (b).

With increasing cellulose formate content, the temperature of the second degradation peak gradually decreases from 275 °C (100 Silk) to 245 °C (10:90 SC). This indicates that with increasing cellulose formate, the overall thermal stability of the composite diminishes. There is no consistent trend related to the degradation temperature of cellulose formate in the sample, but it ranges from 160 – 180 °C. In Figure 3.3b, the reversing heat capacity illustrates the glass transition of the samples more clearly. The first T_g indicates the sample with bond water present, and all the samples, except 25:75 SC, have one distinct T_g, suggesting silk and cellulose formate formed a fully miscible blend. 100Silk shows the lowest T_g with bond water at 59.68°C and 25:75SC the highest temperature at 82.60°C.

With the addition of only 10% cellulose formate, the T_g drops significantly, then gradually increases with increasing silk content. From Figure 3.3b, the 10:90 SC has a much smaller heat capacity increment which can indicate its low molecular mobility within the polymer chain. This trend where the molecular mobility decreases with increasing cellulose formate is due to the crystalline structure of cellulose formate. While unclear in the heat flow plot, Figure 3.3b shows the100 Silk sample T_g at ~175°C. For the 25:75 SC sample, there are two glass transition temperatures. The second glass transition temperature matches that of pure silk, which lies at ~178°C [116]. For all other samples, this second T_g, representing silk, is covered by the exothermic degradation peak of cellulose formate which occurs from 160-180 °C.

Figure 3.4

DSC Thermograms of Vertical Silk-CF Nanofibers

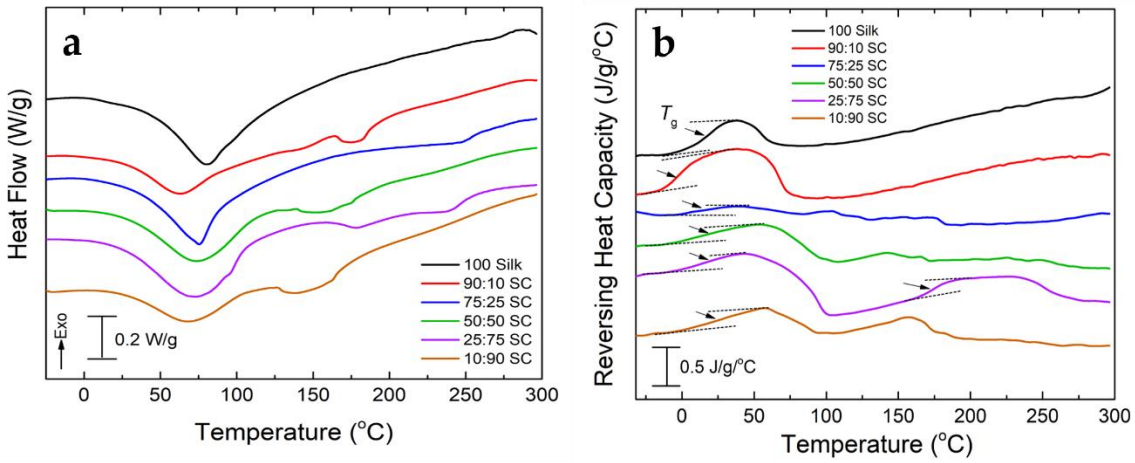

Note. TMDSC plots of vertically electrospun silk-CF composites after water annealing. Heat flow is shown in (a) and reversing heat capacity is shown in (b).

Table 3.1

DSC Thermal Analysis for Horizontal and Vertical Electrospun Silk-Cellulose Formate Nanofibers

Sample	**T_g(°C)**	**T_s(°C)**	**$T_{d(}$°C)**
Horizontal 100Silk	167.85	63.67	262.83
Vertical 100Silk	170.13	80.52	212.81
Horizontal 9010SC	187.74	57.93	263.62
Vertical 9010SC	144.63	62.67	204.19

Sample	T_g(ºC)	T_s(ºC)	T_d(ºC)
Horizontal 7525SC	107.95	65.46	274.60
Vertical 7525SC	160.34	75.62	177.81
Horizontal 5050SC	225.39	109.22	263.41
Vertical 5050SC	128.15	79.28	171.81
Horizontal 2575SC	225.14	66.96	263.84
Vertical 2575SC	159.30	74.91	221.03
Horizontal 1090SC	224.35	68.38	164.30
Vertical 1090SC	58.25	73.14	145.64

Note. TMDSC comparison of electrospun nanofibers where T_g is the glass transition temperature, T_s is the bound solvent release peak temperature, and T_d is the degradation peak temperature. All numbers have an error bar within ±5%.

The TMDSC for the vertically spun nanofibers is shown in Figure 3.4. In Figure 3.4a, there is an initial peak at around 60-75°C for the solvent evaporation and glass transition of the composites. Unlike the horizontal sample, the vertical samples do not show a clear, two-step degradation process for all the composite samples. This may be due to noise within the data, as some samples only show a silk peak while others only show a cellulose formate peak. As seen horizontally, the degradation temperature of samples with decreasing silk content decreases with increasing cellulose formate when

comparing the 100 Silk, 75:25 SC, and 25:75 SC samples to one another. In addition, the cellulose formate degradation ranges from 150-175 ℃. Fig. 3.4b indicates that the vertically spun fibers follow the same basic trends seen horizontally.

3.3.3 Thermal Gravimetric Analysis (TGA)

The thermogravimetric (TG) analysis provides direct evidence of polymer thermal decomposition, composition, and purity. The thermal stability statistics show all twelve silk-cellulose formate composite nanofiber samples onset and end temperatures, weight-loss percentage, $T_{\Delta max}$ or maximum degradation peak, bound solvent content percentage, and thermal degradation at 600°C. Utilizing Figure 3.5, the resulting values from these analyses are displayed in Tables 3.2 and 3.3. Firstly, the horizontal nanofibers onset temperatures of decomposition range from 170 ℃ for 10:90 SC to around 300 ℃ for silk dominant samples. Figure 3.5a indicates that the 90:10 SC sample has the highest thermal stability of all the samples, retaining about 87% of its remaining mass at 600 °C. Surprisingly, 100 Silk has less remaining mass at 600°C at around 41%.

While higher silk content is generally associated with greater thermal stability due to silk's backbone, this data verifies that blending silk with cellulose formate increases the thermal properties of pure silk. When referring to the graph of derivative weight percent vs temperature (Fig. 3.5b), all the horizontal fibers show a clear endothermic peak representing the evaporation of bound solvents from the nanofibers. All horizontal fibers have a slight decrease (ranging from 1-9%) in mass that can be observed at ~ 45°C due to the above-mentioned entrapped solvent or moisture.

In Figure 3.5b, the horizontal composite fibers show two distinct max degradation peaks, $T_{\Delta max}$, after the solvent evaporation peak apart from 10:90SC which has 3 clear degradation peaks. Similarly, the 25:75SC sample has a slight shoulder, giving it a 3rd maximum decomposition peak at 350°C. The 10:90SC trimodal thermogram has the first and second max degradation peaks at 208.50°C and 260.09°C. As the cellulose formate content increases, these peaks increase in intensity, confirming the composition of these samples belong mainly to cellulose formate. Whereas the third peak at 366.28 °C can be explained by silk, which degrades at a higher temperature due to silk's polypeptide backbone. The graph shows that increasing the cellulose formate content in the fibers shifts the T_{Δ}max for the silk components to a higher temperature. For instance, 100 Silk has a $T_{\Delta max}$ at 332.24 °C, and 10:90 SC has a $T_{\Delta max}$ at 366.28 °C. This verifies that blending with cellulose formate helps to enhance the thermal properties of silk, making it more thermally stable than 100 Silk.

The vertically spun nanofibers share similarities with those spun horizontally, but they also differ in a few aspects. Like the horizontal fibers, the vertical samples also show an initial mass loss at ~50 °C due to solvent evaporation. However, the decrease in mass is slightly higher (15-18%). This signifies the ability of the vertically electrospun fibers to retain more moisture. We can assume, given the SEM results, that the fiber morphology plays a role. In this case, the branching and coil fiber network can absorb and retain a significant amount more of solvent in their matrix. Another key difference is that the degradation of the silk backbone is stronger in the vertical 90:10 SC sample than it is in

the horizontal direction due to the significant mass remaining difference between the two samples.

However, the data in Table 3.3 shows that the vertical fibers are less thermally stable than the horizontal fibers, especially in the silk dominant samples. The onset temperatures of decomposition for silk dominant samples are slightly lower for the same blend ratios horizontally. For example, the 90:10SC sample sits at 215.09 °C compared to 239.62 °C for the horizontal setup, indicating less thermal stability in the vertical nanofibers. In addition, the vertically spun 90:10 SC and 75:25 SC samples have much less mass remaining at 600 °C when compared to their counterpart.

While the 90:10 SC horizontal sample had the highest remaining mass at 87.56%, the 90:10 SC vertical had one of the lowest remaining masses at around 40%. Surprisingly, even though the 50:50 SC samples in both orientations had no significant difference in the percent mass remaining at 600°C (56.05% horizontal, 56.94% vertical), the 50:50 SC vertical nanofibers are the most thermally stable for the vertical samples. Due to the thermal instability of the composite samples, the vertical 100 Silk is superior to all samples except 50:50 SC. This significant decrease in the thermal stability of the composite fibers in the vertical direction may be due to the coiling and branching. While 50:50 SC is an exception, it is possibly due to strong interactions between silk and cellulose formate when combined in a 1:1 ratio. Additionally, the 50:50 SC in both setups show no significant difference in the two distinct degradation peaks after the solvent evaporation. Compared to the vertical 75:25 SC sample, however, the 2nd endothermic

peak in the horizontal 75:25 SC sample shifted to the right with the increase in cellulose formate content.

Figure 3.5

TGA Thermograms of Silk-Cellulose Formate Nanofibers

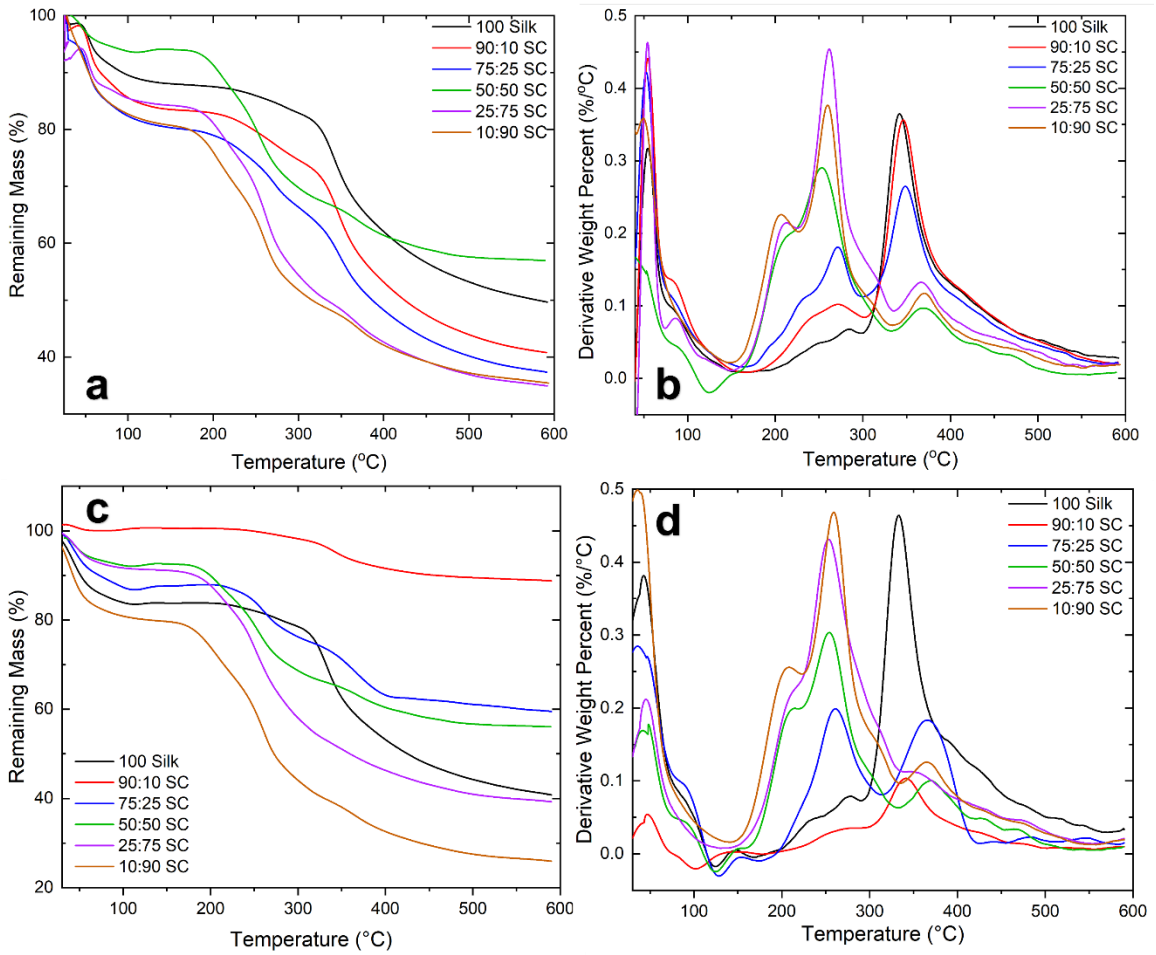

Note. Thermogravimetric plots of horizontally electrospun Silk-CF samples. The percent mass remaining with respect to temperature mass remaining is shown in (a) and the rate at which the samples were degraded in (b). The TGA plots of vertically electrospun Silk-CF samples are shown in (c) the percent mass remaining with respect to temperature and (d) the rate at which the samples were degraded.

Table 3.2

Thermal Analysis of Horizontal Silk- Cellulose Formate Nanofibers

Sample	**Td_1 (ºC)**	**Δm_1 (%)**	**Td_2 (ºC)**	**Δm_2 (%)**	**Bound Solvent (%)**	**Td_{end} (ºC)**	**$T_{\Delta max}$ (ºC)**	**m_{f600} (%)**
100 Silk	303.90	39.44	--	--	14.97	367.79	332.84	40.81
90:10 SC	239.62	8.16	--	--	1.28	368.70	288.94, 339.40	87.56
75:25 SC	233.87	12.06	274.94	12.69	12.31	392.44	260.95, 367.46	59.50
50:50 SC	215.50	23.28	269.86	12.25	7.97	401.19	252.97, 358.38	56.05
25:75 SC	159.91	18.54	260.09	15.25	8.17	328.37	211.77, 251.94, 350.02	39.25
10:90 SC	172.29	28.57	270.04	16.89	18.85	389.30	208.50, 260.09, 366.28	25.93

*Not*e. TGA analysis displaying the Initial temperature (onset) of decomposition (Tdi), relative % loss of mass Δm_i of the two steps mainly related with cellulose decomposition and silk decomposition, bound solvent content percentage, the final temperature of decomposition (Td_{end}), maximum temperature of the derivative ($T_{\Delta max}$), and the relative final mass at 600ºC(mf600).

Table 3.3

Thermal Analysis of Vertical Silk-Cellulose Formate Nanofibers

Sample	**Td_1 (ºC)**	**Δm_1 (%)**	**Td_2 (ºC)**	**Δm_2 (%)**	**Bound Solvent (%)**	**Td_{end} (ºC)**	**$T_{\Delta max}$ (ºC)**	**m_{f600} (%)**
100 Silk	312.53	33.70	--	--	12.28	378.01	341.81	49.64
90:10 SC	215.09	29.26	--	--	16.12	274.8	271.63, 344.99	40.75
75:25 SC	228.59	13.62	281.58	18.90	18.26	369.88	271.47, 347.73	37.34
50:50 SC	209.54	26.26	277.35	7.65	5.91	390.82	254.83, 368.11	56.94
25:75 SC	179.19	28.30	269.32	15.13	15.56	394.19	261.30, 367.68	34.90
10:90 SC	172.26	21.79	271.82	12.77	18.89	383.42	204.26, 259.81, 370.32	35.40

Note. TGA analysis displaying the Initial temperature (onset) of decomposition (Tdi), relative % loss of mass (Δm_i) of the two steps mainly related with cellulose decomposition and silk decomposition, bound solvent content percentage, the final temperature of decomposition (Td_{end}), maximum temperature of the derivative ($T_{\Delta max}$), and the relative final mass at 600ºC (mf600).

3.3.4 Morphology Analysis

The SEM images for the horizontally spun silk-cellulose formate nanofibers, depicted in Figure 3.6, provide insight into how the blend ratio impacts the morphology and structure of the fibers. The pure silk sample (100 Silk) spun thin, relatively homogenous nanofibers that appear to possess the desirable mechanical properties of silk (i.e., flexibility, mechanical strength). On the other hand, the pure cellulose formate sample (100 CF) did not form rigid nanofibers but formed fibers with clumpy aggregates. 100 CF likely did not form rigid nanofibers due to residual cellulose that did not react with the formic acid and remained undissolved in solution.

In the composite nanofibers, there is a general trend where samples with higher SF content appear more rigid and mechanically strong. This can likely be explained by SF's high beta sheet content which grants it desirable mechanical properties. As the SF content decreases, the nanofibers appear more wavy, curly, and elastic. Formation of wavy nanofibers can be clearly seen in the 25:75 SC and 10:90 SC nanofibers. The trend appears to be disrupted when comparing the 75:25 SC nanofibers to the 50:50 SC nanofibers, as the 50:50 SC nanofibers appear more straight and rigid despite their lower SF content. All the samples did not display high degrees of coiling and branching, if any.

The SEM images for the vertically spun silk-cellulose formate nanofibers are shown in Figure 3.7. Just as in the horizontally spun fibers, a general trend can be observed where when the SF content decreases, the elasticity of the fibers increases. However, unlike the horizontal direction, the vertical SEM images shows coiled and

branched nanofibers. This coiled morphology in the vertical direction can be seen in all blend ratios containing at least 50% CF. Nanofiber coiling is most apparent when comparing the 50:50 SC blend ratios; while the horizontal direction produced conventional, straight fibers, the vertical direction showed a coil-like morphology.

The vertical direction also has an increase in nanofiber branching. Clear examples of branching can be seen in 100 Silk and 10:90 SC. A coiled morphology is likely seen in these vertical samples because of two cooccurring factors. For one, there may have been increased conductivity of formic acid due to the calcium chloride salt creating gaps during the spinning process. Moreover, coils are likely due to an alpha-helical structure being formed between silk and cellulose formate [100]. Nanofiber branching is possibly due to the added gravitational force by spinning in the vertical direction, forming unstable undulation sites along the surface of the polymer jet [95, 99].

Figure 3.6

SEM Images of Horizontal Silk-CF Nanofibers

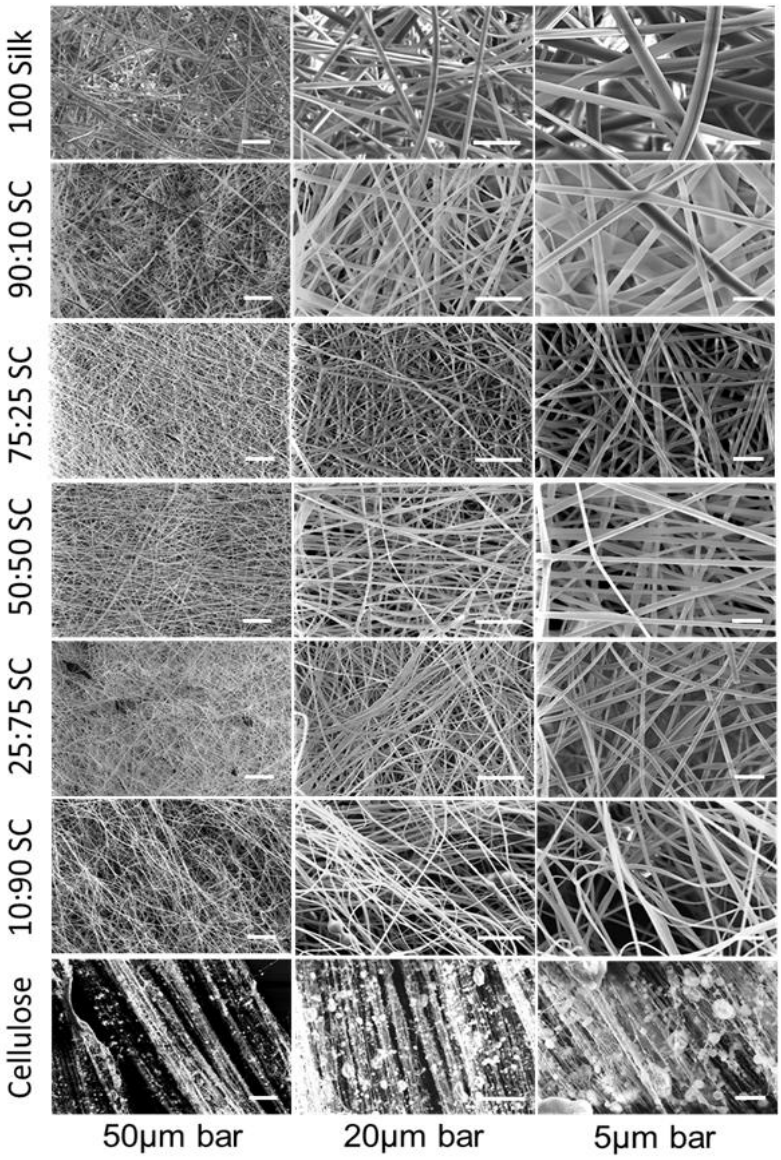

Note. SEM images of electrospun blends of silk and cellulose formate in the horizontal direction.

Figure 3.7

SEM Images of Vertical Silk-CF Nanofibers

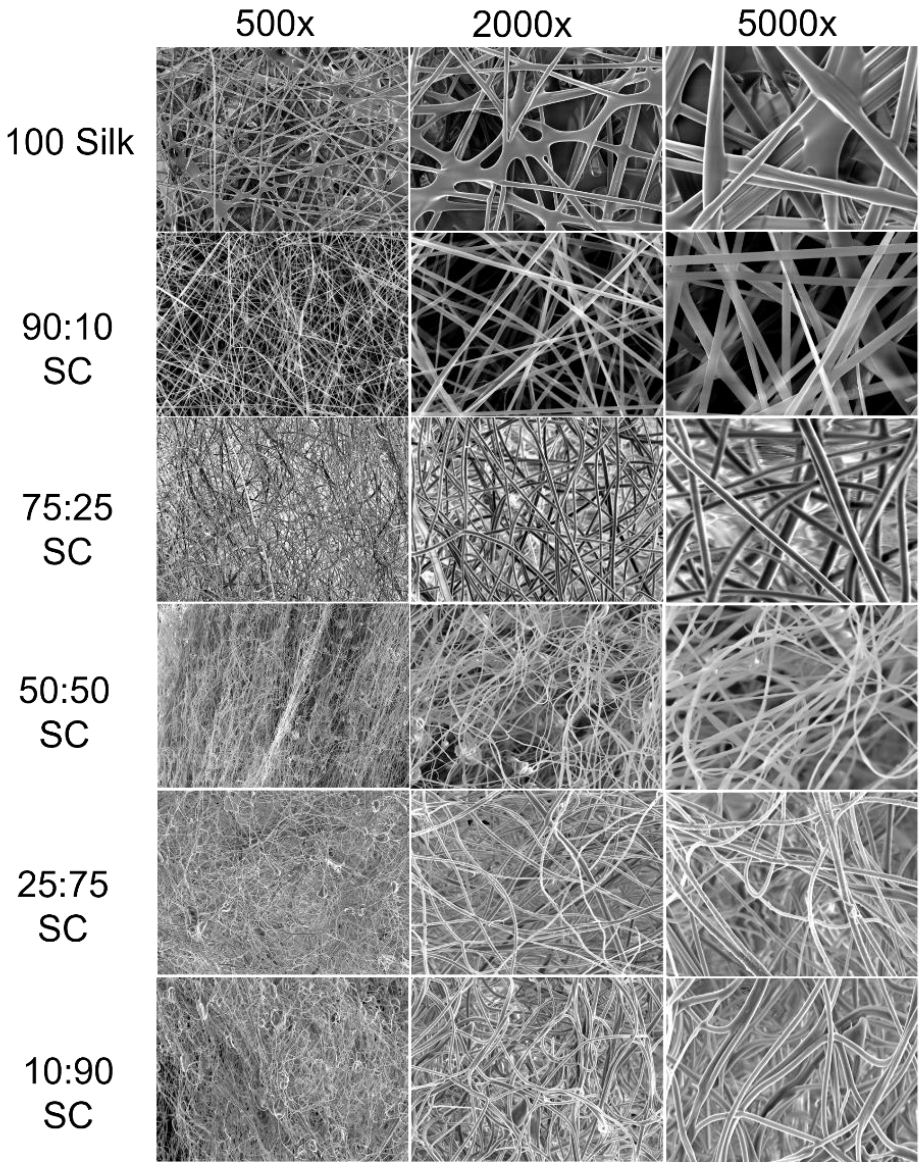

Note. SEM images of electrospun blends of silk and cellulose formate in the vertical direction.

3.3.5 Mechanism of Interaction

There are a few proposed explanations for why coiled and branched nanofibers are forming in the vertical direction. The FTIR data for the vertical nanofibers verifies that as the cellulose formate content increases, a more alpha helical structure is favored in the nanofibers. Silk already has an alpha helical structure due to intramolecular hydrogen bonding between the -NH groups and C=O groups within silk. This increased alpha helical structure could be due to intermolecular hydrogen bonding between formyl groups in cellulose formate and functional groups within silk.

Coils are likely due to an alpha-helical structure being formed between silk and cellulose formate. This may explain why vertical samples with more cellulose formate displayed more coiling. Coil formation may have also been favored because of an increased conductivity of formic acid due to the calcium chloride salt creating gaps during the spinning process. Nanofiber branching possibly occurred due to the added gravitational force by spinning in the vertical direction, forming unstable undulation sites along the surface of the polymer jet.

Figure 3.8

Mechanism of Interaction

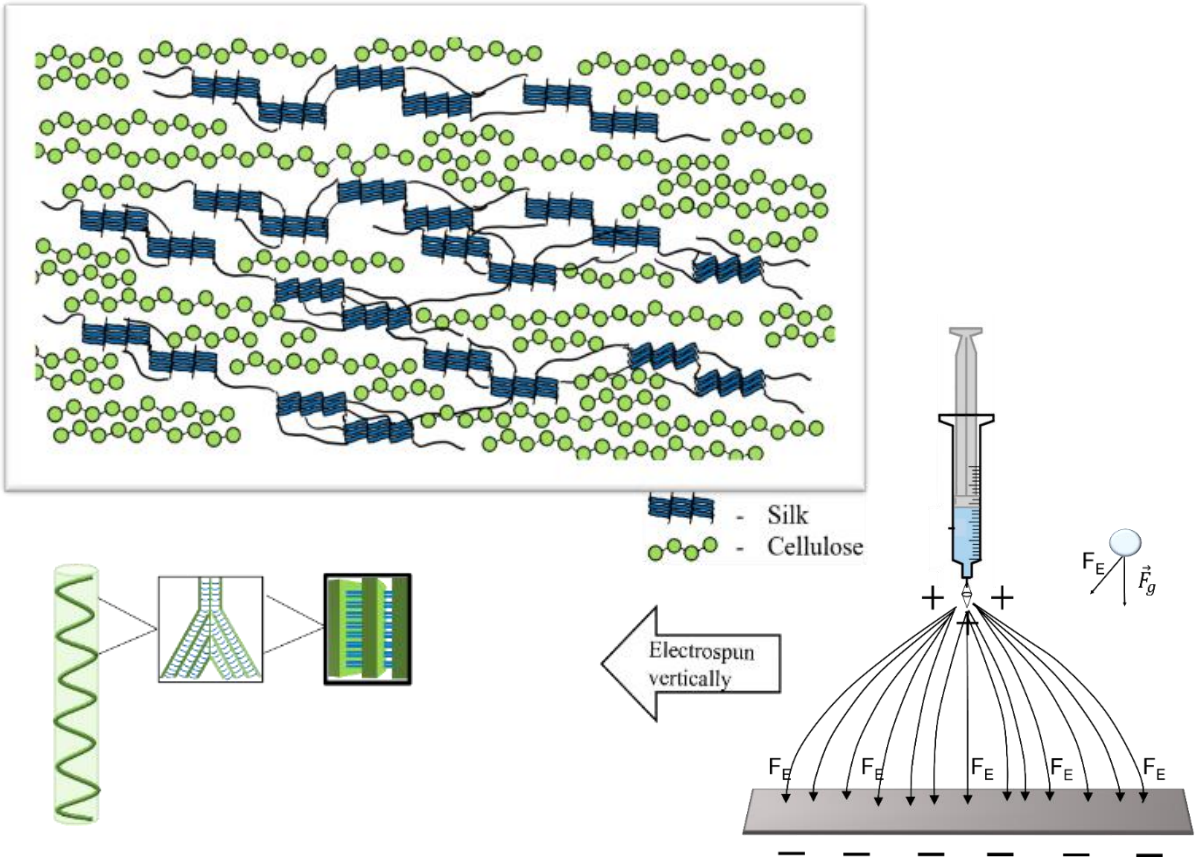

Note. Schematic describing the fabrication mechanism during electrospinning.

3.4 Conclusions

This work presents the first reported fabrication and analysis of silk-cellulose formate nanofibers spun in the horizontal and vertical directions. In both spinning orientations, silk-dominant nanofibers appeared rigid and mechanically strong, while cellulose formate dominant fibers appeared more elastic. We found that electrospinning in the horizontal direction forms straight, conventional fibers, and electrospinning in the vertical direction forms coiled and branched fibers. In both the horizonal and vertical direction, the FTIR data indicates that silk adopts an alpha helical secondary structure with the addition of cellulose formate.

We hypothesize that this alpha helical structure contributes to nanofiber coiling when spun vertically. Being able to select for coiled and branched polymers by spinning in the vertical direction is a useful innovation that holds promise in the field of tissue engineering and regenerative medicine. While the vertically spun nanofibers possess a morphological advantage, the TG analysis indicated they were less thermally stable than those spun horizontally. We believe our work presents the fabrication of extremely tunable nanofibers due to the convertibility of cellulose formate and the influence of blend ratio and spinning direction on their morphological, structural, and thermal properties.

References

1. Azevedo, M.; Reis, R.; Claase, M.; Grijpma, D.; Feijen, J., Development and properties of polycaprolactone/hydroxyapatite composite biomaterials. *Journal of materials science: Materials in medicine* **2003,** *14* (2), 103-107.

2. Zheng, Y.; Monty, J.; Linhardt, R. J., Polysaccharide-based nanocomposites and their applications. *Carbohydrate research* **2015,** *405*, 23-32.

3. Suh, J.-K. F.; Matthew, H. W., Application of chitosan-based polysaccharide biomaterials in cartilage tissue engineering: a review. *Biomaterials* **2000,** *21* (24), 2589-2598.

4. Miao, J.; Pangule, R. C.; Paskaleva, E. E.; Hwang, E. E.; Kane, R. S.; Linhardt, R. J.; Dordick, J. S., Lysostaphin-functionalized cellulose fibers with antistaphylococcal activity for wound healing applications. *Biomaterials* **2011,** *32* (36), 9557-9567.

5. Liu, L.; Liu, L.; Liu, C.-K.; Fishman, M. L.; Hicks, K. B., Composite films from pectin and fish skin gelatin or soybean flour protein. *Journal of agricultural and food chemistry* **2007,** *55* (6), 2349-2355.

6. Hu, X.; Cebe, P.; Weiss, A. S.; Omenetto, F.; Kaplan, D. L., Protein-based composite materials. *Materials today* **2012,** *15* (5), 208-215.

7. Hardy, J. G.; Römer, L. M.; Scheibel, T. R., Polymeric materials based on silk proteins. *Polymer* **2008,** *49* (20), 4309-4327.

8. Parambath, A., *Engineering of biomaterials for drug delivery systems: beyond polyethylene glycol*. Woodhead Publishing: 2018.

9. Zhang, Z.; Ortiz, O.; Goyal, R.; Kohn, J., Handbook of Polymer Applications in Medicine and Medical Devices: 13. Biodegradable Polymers. **2013**.

10. Gagner, J. E.; Kim, W.; Chaikof, E. L., Designing protein-based biomaterials for medical applications. *Acta biomaterialia* **2014,** *10* (4), 1542-1557.

11. Bealer, E. J.; Kavetsky, K.; Dutko, S.; Lofland, S.; Hu, X., Protein and polysaccharide-based magnetic composite materials for medical applications. *International journal of molecular sciences* **2020,** *21* (1), 186.

12. Wang, F.; Wu, H.; Venkataraman, V.; Hu, X., Silk fibroin-poly(lactic acid) biocomposites: Effect of protein-synthetic polymer interactions and miscibility on material properties and biological responses. *Materials Science and Engineering: C* **2019,** *104*, 109890.

13. Xue, Y.; Wang, F.; Torculas, M.; Lofland, S.; Hu, X., Formic Acid Regenerated Mori, Tussah, Eri, Thai, and Muga Silk Materials: Mechanism of Self-Assembly. *ACS Biomaterials Science & Engineering* **2019,** *5* (12), 6361-6373.

14. Callaway, K. A.; Xue, Y.; Altimari, V.; Jiang, G.; Hu, X., Comparative investigation of thermal and structural behavior in renewably sourced composite films of even-even nylons (610 and 1010) with silk fibroin. *Polymers* **2018,** *10* (9), 1029.

15. Hu, X.; Kaplan, D.; Cebe, P., Determining Beta-Sheet Crystallinity in Fibrous Proteins by Thermal Analysis and Infrared Spectroscopy. *Macromolecules* **2006,** *39* (18), 6161-6170.

16. Dumitriu, S., *Polysaccharides: structural diversity and functional versatility*. CRC press: 2004.

17. Stanton, J.; Xue, Y.; Pandher, P.; Malek, L.; Brown, T.; Hu, X.; Salas-de la Cruz, D., Impact of ionic liquid type on the structure, morphology and properties of silk-cellulose biocomposite materials. *International Journal of Biological Macromolecules* **2018,** *108*, 333-341.

18. Coma, V., Polysaccharide-based biomaterials with antimicrobial and antioxidant properties. *Polímeros* **2013,** *23*, 287-297.

19. Dassanayake, R. S.; Acharya, S.; Abidi, N., Biopolymer-based materials from polysaccharides: properties, processing, characterization and sorption applications, in: advanced sorption process applications. *IntechOpen.* **2019**.

20. Aspinall, G. O., *The polysaccharides*. Academic Press: 2014.

21. Yalpani, M., *Polysaccharides: syntheses, modifications and structure/property relations*. Elsevier: 2013.

22. BeMiller, J. N., Polysaccharides: Occurrence, Significance, and Properties. In *Glycoscience: Chemistry and Chemical Biology*, Fraser-Reid, B. O.; Tatsuta, K.; Thiem, J., Eds. Springer Berlin Heidelberg: Berlin, Heidelberg, 2008; pp 1413-1435.

23. Crini, G., Recent developments in polysaccharide-based materials used as adsorbents in wastewater treatment. *Progress in polymer science* **2005,** *30* (1), 38-70.

24. Stanton, J.; Xue, Y.; Waters, J. C.; Lewis, A.; Cowan, D.; Hu, X.; la Cruz, D. S.-d., Structure–property relationships of blended polysaccharide and protein biomaterials in ionic liquid. *Cellulose (London)* **2017,** *24* (4), 1775-1789.

25. Hadadi, A.; Whittaker, J. W.; Verrill, D. E.; Hu, X.; Larini, L.; Salas-De La Cruz, D., A hierarchical model to understand the processing of polysaccharides/protein-based films in ionic liquids. *Biomacromolecules* **2018,** *19* (10), 3970-3982.

26. Love, S. A.; Popov, E.; Rybacki, K.; Hu, X.; Salas-de la Cruz, D., Facile treatment to fine-tune cellulose crystals in cellulose-silk biocomposites through hydrogen peroxide. *International Journal of Biological Macromolecules* **2020,** *147,* 569-575.

27. Shang, S.; Zhu, L.; Fan, J., Intermolecular interactions between natural polysaccharides and silk fibroin protein. *Carbohydrate polymers* **2013,** *93* (2), 561-573.

28. Blessing, B.; Trout, C.; Morales, A.; Rybacki, K.; Love, S. A.; Lamoureux, G.; O'Malley, S. M.; Hu, X.; Salas-de la Cruz, D., Morphology and ionic conductivity relationship in silk/cellulose biocomposites. *Polymer International* **2019,** *68* (9), 1580-1590.

29. Chen, L.; Remondetto, G. E.; Subirade, M., Food protein-based materials as nutraceutical delivery systems. *Trends in Food Science & Technology* **2006,** *17* (5), 272-283.

30. Jones, O. G.; Decker, E. A.; McClements, D. J., Comparison of protein–polysaccharide nanoparticle fabrication methods: Impact of biopolymer complexation before or after particle formation. *Journal of Colloid and Interface Science* **2010,** *344* (1), 21-29.

31. Chen, Y. L.; Fan, K. T.; Hung, S. C.; Chen, Y. R., The role of peptides cleaved from protein precursors in eliciting plant stress reactions. *New Phytologist* **2020,** *225* (6), 2267-2282.

32. Thinakaran, G.; Koo, E. H., Amyloid precursor protein trafficking, processing, and function. *Journal of Biological Chemistry* **2008,** *283* (44), 29615-29619.

33. Kundu, B.; Kurland, N. E.; Bano, S.; Patra, C.; Engel, F. B.; Yadavalli, V. K.; Kundu, S. C., Silk proteins for biomedical applications: Bioengineering perspectives. *Progress in polymer science* **2014,** *39* (2), 251-267.

34. Altman, G. H.; Diaz, F.; Jakuba, C.; Calabro, T.; Horan, R. L.; Chen, J.; Lu, H.; Richmond, J.; Kaplan, D. L., Silk-based biomaterials. *Biomaterials* **2003,** *24* (3), 401-416.

35. Vepari, C.; Kaplan, D. L., Silk as a biomaterial. *Progress in Polymer Science* **2007,** *32* (8), 991-1007.

36. Rouse, J. G.; Van Dyke, M. E., A review of keratin-based biomaterials for biomedical applications. *Materials* **2010,** *3* (2), 999-1014.

37. Lee, H.; Noh, K.; Lee, S. C.; Kwon, I.-K.; Han, D.-W.; Lee, I.-S.; Hwang, Y.-S., Human hair keratin and its-based biomaterials for biomedical applications. *Tissue Engineering and Regenerative Medicine* **2014,** *11* (4), 255-265.

38. Vasconcelos, A.; Cavaco-Paulo, A., The use of keratin in biomedical applications. *Current drug targets* **2013,** *14* (5), 612-619.

39. Wool, R.; Sun, X. S., *Bio-Based Polymers and Composites*. Elsevier Science: 2011.

40. Singh, P.; Kumar, R.; Sabapathy, S.; Bawa, A., Functional and edible uses of soy protein products. *Comprehensive reviews in food science and food safety* **2008,** *7* (1), 14-28.

41. Kumar, R.; Wang, L.; Zhang, L., Structure and mechanical properties of soy protein materials plasticized by thiodiglycol. *Journal of applied polymer science* **2009,** *111* (2), 970-977.

42. Lu, Y.; Weng, L.; Zhang, L., Morphology and properties of soy protein isolate thermoplastics reinforced with chitin whiskers. *Biomacromolecules* **2004,** *5* (3), 1046-1051.

43. Corradini, E.; Curti, P. S.; Meniqueti, A. B.; Martins, A. F.; Rubira, A. F.; Muniz, E. C., Recent advances in food-packing, pharmaceutical and biomedical applications of zein and zein-based materials. *International journal of molecular sciences* **2014,** *15* (12), 22438-22470.

44. Shukla, R.; Cheryan, M., Zein: the industrial protein from corn. *Industrial crops and products* **2001,** *13* (3), 171-192.

45. Liu, D.; Nikoo, M.; Boran, G.; Zhou, P.; Regenstein, J. M., Collagen and gelatin. *Annual review of food science and technology* **2015,** *6*, 527-557.

46. Abou Neel, E. A.; Bozec, L.; Knowles, J. C.; Syed, O.; Mudera, V.; Day, R.; Hyun, J. K., Collagen—emerging collagen based therapies hit the patient. *Advanced drug delivery reviews* **2013,** *65* (4), 429-456.

47. Gómez-Guillén, M.; Giménez, B.; López-Caballero, M. a.; Montero, M., Functional and bioactive properties of collagen and gelatin from alternative sources: A review. *Food hydrocolloids* **2011,** *25* (8), 1813-1827.

48. Olsen, D.; Yang, C.; Bodo, M.; Chang, R.; Leigh, S.; Baez, J.; Carmichael, D.; Perälä, M.; Hämäläinen, E.-R.; Jarvinen, M., Recombinant collagen and gelatin for drug delivery. *Advanced drug delivery reviews* **2003,** *55* (12), 1547-1567.

49. Rnjak-Kovacina, J.; Wise, S. G.; Li, Z.; Maitz, P. K.; Young, C. J.; Wang, Y.; Weiss, A. S., Electrospun synthetic human elastin: collagen composite scaffolds for dermal tissue engineering. *Acta biomaterialia* **2012,** *8* (10), 3714-3722.

50. Barreto, M.; Jedlicki, E.; Holmes, D. S., Identification of a gene cluster for the formation of extracellular polysaccharide precursors in the chemolithoautotroph Acidithiobacillus ferrooxidans. *Applied and environmental microbiology* **2005,** *71* (6), 2902-2909.

51. Seitz, B.; Klos, C.; Wurm, M.; Tenhaken, R., Matrix polysaccharide precursors in Arabidopsis cell walls are synthesized by alternate pathways with organ‐specific expression patterns. *The Plant Journal* **2000,** *21* (6), 537-546.

52. Lindahl, U.; Li, J.-p.; Kusche-Gullberg, M.; Salmivirta, M.; Alaranta, S.; Veromaa, T.; Emeis, J.; Roberts, I.; Taylor, C.; Oreste, P., Generation of "Neoheparin" from E. c oli K5 Capsular Polysaccharide. *Journal of medicinal chemistry* **2005,** *48* (2), 349-352.

53. Torres, F. G.; Commeaux, S.; Troncoso, O. P., Biocompatibility of bacterial cellulose based biomaterials. *Journal of Functional Biomaterials* **2012,** *3* (4), 864-878.

54. Modulevsky, D. J.; Cuerrier, C. M.; Pelling, A. E., Biocompatibility of subcutaneously implanted plant-derived cellulose biomaterials. *PloS one* **2016,** *11* (6), e0157894.

55. Peng, X.-w.; Ren, J.-l.; Zhong, L.-x.; Sun, R.-c., Nanocomposite films based on xylan-rich hemicelluloses and cellulose nanofibers with enhanced mechanical properties. *Biomacromolecules* **2011,** *12* (9), 3321-3329.

56. Fricain, J.; Granja, P.; Barbosa, M.; De Jéso, B.; Barthe, N.; Baquey, C., Cellulose phosphates as biomaterials. In vivo biocompatibility studies. *Biomaterials* **2002,** *23* (4), 971-980.

57. Rinaudo, M., Chitin and chitosan: Properties and applications. *Progress in polymer science* **2006,** *31* (7), 603-632.

58. Safarik, I.; Pospiskova, K.; Baldikova, E.; Savva, I.; Vekas, L.; Marinica, O.; Tanasa, E.; Krasia-Christoforou, T., Fabrication and bioapplications of magnetically modified chitosan-based electrospun nanofibers. *Electrospinning* **2018,** *2* (1), 29-39.

59. Cheba, B. A., Chitin and chitosan: marine biopolymers with unique properties and versatile applications. *Global Journal of Biotechnology & Biochemistry* **2011,** *6* (3), 149-153.

60. Wang, B.-L.; Liu, X.-S.; Ji, Y.; Ren, K.-F.; Ji, J., Fast and long-acting antibacterial properties of chitosan-Ag/polyvinylpyrrolidone nanocomposite films. *Carbohydrate polymers* **2012,** *90* (1), 8-15.

61. Lewis, A.; Waters, J. C.; Stanton, J.; Hess, J.; Salas-De La Cruz, D., Macromolecular interactions control structural and thermal properties of regenerated tri-component blended films. *International journal of molecular sciences* **2016,** *17* (12), 1989.

62. Cox, P., Kirk-Othmer encyclopedia of chemical technology. *Talanta* **1996,** *5* (43), 805.

63. Torres, F. G.; Commeaux, S.; Troncoso, O. P., Starch‐based biomaterials for wound‐dressing applications. *Starch‐Stärke* **2013,** *65* (7‐8), 543-551.

64. Mozafari, M. R., *Nanomaterials and nanosystems for biomedical applications*. Springer Science & Business Media: 2007.

65. Voragen, A. G. J.; Coenen, G.-J.; Verhoef, R. P.; Schols, H. A., Pectin, a versatile polysaccharide present in plant cell walls. *Structural Chemistry* **2009,** *20* (2), 263.

66. Mohnen, D., Pectin structure and biosynthesis. *Current opinion in plant biology* **2008,** *11* (3), 266-277.

67. Noreen, A.; Akram, J.; Rasul, I.; Mansha, A.; Yaqoob, N.; Iqbal, R.; Tabasum, S.; Zuber, M.; Zia, K. M., Pectins functionalized biomaterials; a new viable approach for biomedical applications: A review. *International journal of biological macromolecules* **2017,** *101*, 254-272.

68. Mishra, R.; Banthia, A.; Majeed, A., Pectin based formulations for biomedical applications: a review. *Asian Journal of Pharmaceutical and Clinical Research* **2012,** *5* (4), 1-7.

69. Zha, F.; Chen, W.; Zhang, L.; Yu, D., Electrospun natural polymer and its composite nanofibrous scaffolds for nerve tissue engineering. *Journal of Biomaterials Science, Polymer Edition* **2020,** *31* (4), 519-548.

70. Wsoo, M. A.; Shahir, S.; Mohd Bohari, S. P.; Nayan, N. H. M.; Razak, S. I. A., A review on the properties of electrospun cellulose acetate and its application in drug delivery systems: A new perspective. *Carbohydrate Research* **2020,** *491*, 107978.

71. Jacob, J.; Haponiuk, J. T.; Thomas, S.; Gopi, S., Biopolymer based nanomaterials in drug delivery systems: A review. *Materials Today Chemistry* **2018,** *9*, 43-55.

72. Kundu, S., *Silk Biomaterials for Tissue Engineering and Regenerative Medicine*. Elsevier Science & Technology: Cambridge, UNITED KINGDOM, 2014.

73. Malafaya, P. B.; Silva, G. A.; Reis, R. L., Natural–origin polymers as carriers and scaffolds for biomolecules and cell delivery in tissue engineering applications. *Advanced Drug Delivery Reviews* **2007,** *59* (4), 207-233.

74. Dal Pra, I.; Freddi, G.; Minic, J.; Chiarini, A.; Armato, U., De novo engineering of reticular connective tissue in vivo by silk fibroin nonwoven materials. *Biomaterials* **2005,** *26* (14), 1987-1999.

75. Horan, R. L.; Antle, K.; Collette, A. L.; Wang, Y.; Huang, J.; Moreau, J. E.; Volloch, V.; Kaplan, D. L.; Altman, G. H., In vitro degradation of silk fibroin. *Biomaterials* **2005,** *26* (17), 3385-3393.

76. Keten, S.; Xu, Z.; Ihle, B.; Buehler, M. J., Nanoconfinement controls stiffness, strength and mechanical toughness of β-sheet crystals in silk. *Nature Materials* **2010,** *9* (4), 359-367.

77. Swapnil, S. I.; Datta, N.; Mahmud, M. M.; Jahan, R. A.; Arafat, M. T., Morphology, mechanical, and physical properties of wet-spun cellulose acetate fiber in different solvent-coagulant systems and in-situ crosslinked environment. *Journal of Applied Polymer Science* **2021,** *138* (18), 50358.

78. Liu, X.; Lin, T.; Gao, Y.; Xu, Z.; Huang, C.; Yao, G.; Jiang, L.; Tang, Y.; Wang, X., Antimicrobial electrospun nanofibers of cellulose acetate and polyester urethane composite for wound dressing. *Journal of Biomedical Materials Research Part B: Applied Biomaterials* **2012,** *100B* (6), 1556-1565.

79. Crabbe-Mann, M.; Tsaoulidis, D.; Parhizkar, M.; Edirisinghe, M., Ethyl cellulose, cellulose acetate and carboxymethyl cellulose microstructures prepared using electrohydrodynamics and green solvents. *Cellulose* **2018,** *25* (3), 1687-1703.

80. Unnithan, A. R.; Gnanasekaran, G.; Sathishkumar, Y.; Lee, Y. S.; Kim, C. S., Electrospun antibacterial polyurethane–cellulose acetate–zein composite mats for wound dressing. *Carbohydrate Polymers* **2014,** *102*, 884-892.

81. Nobile, S.; Nobile, L., Nanotechnology for biomedical applications: Recent advances in neurosciences and bone tissue engineering. *Polymer Engineering & Science* **2017,** *57* (7), 644-650.

82. Yin, J.; Fan, H.; Zhou, J., Cellulose acetate/poly(vinyl alcohol) and cellulose acetate/crosslinked poly(vinyl alcohol) blend membranes: preparation, characterization, and antifouling properties. *Desalination and Water Treatment* **2016,** *57* (23), 10572-10584.

83. Ahmed, M. K.; Menazea, A. A.; Abdelghany, A. M., Blend biopolymeric nanofibrous scaffolds of cellulose acetate/ε-polycaprolactone containing metallic nanoparticles prepared by laser ablation for wound disinfection applications. *International Journal of Biological Macromolecules* **2020,** *155*, 636-644.

84. Liao, N.; Unnithan, A. R.; Joshi, M. K.; Tiwari, A. P.; Hong, S. T.; Park, C.-H.; Kim, C. S., Electrospun bioactive poly (ε-caprolactone)–cellulose acetate–dextran antibacterial composite mats for wound dressing applications. *Colloids and Surfaces A: Physicochemical and Engineering Aspects* **2015,** *469*, 194-201.

85. Kurokawa, N.; Kimura, S.; Hotta, A., Mechanical properties of poly(butylene succinate) composites with aligned cellulose-acetate nanofibers. *Journal of Applied Polymer Science* **2018,** *135* (24), 45429.

86. Xue, J.; Wu, T.; Dai, Y.; Xia, Y., Electrospinning and Electrospun Nanofibers: Methods, Materials, and Applications. *Chem Rev* **2019,** *119* (8), 5298-5415.

87. Stojanov, S.; Berlec, A., Electrospun Nanofibers as Carriers of Microorganisms, Stem Cells, Proteins, and Nucleic Acids in Therapeutic and Other Applications. *Frontiers in bioengineering and biotechnology* **2020,** *8*, 130-130.

88. Huang, S.; Fan, S.; Xie, L.; Wu, Q.; Kong, D.; Wang, Y.; Lim, Y. V.; Ding, M.; Shang, Y.; Chen, S.; Yang, H. Y., Promoting Highly Reversible Sodium Storage of Iron Sulfide Hollow Polyhedrons via Cobalt Incorporation and Graphene Wrapping. *Advanced Energy Materials* **2019,** *9* (33), 1901584.

89. Kim, S. C.; Kang, S.; Lee, H.; Kwak, D.-B.; Ou, Q.; Pei, C.; Pui, D. Y. H., Nanofiber Filter Performance Improvement: Nanofiber Layer Uniformity and Branched Nanofiber. *Aerosol and Air Quality Research* **2020,** *20* (1), 80-88.

90. Zaarour, B.; Zhu, L.; Jin, X., Direct generation of electrospun branched nanofibers for energy harvesting. *Polymers for Advanced Technologies* **2020,** *31* (11), 2659-2666.

91. Zaarour, B.; Zhu, L.; Jin, X., Direct fabrication of electrospun branched nanofibers with tiny diameters for oil absorption. *Journal of Dispersion Science and Technology* **2020**, 1-7.

92. Rodoplu, D.; Mutlu, M., Effects of Electrospinning Setup and Process Parameters on Nanofiber Morphology Intended for the Modification of Quartz Crystal Microbalance Surfaces. *Journal of Engineered Fibers and Fabrics* **2012,** *7* (2), 155892501200700217.

93. Yang, C.; Jia, Z.; Xu, Z.; Wang, K.; Guan, Z.; Wang, L. In *Comparisons of fibers properties between vertical and horizontal type electrospinning systems*, 2009 IEEE Conference on Electrical Insulation and Dielectric Phenomena, 18-21 Oct. 2009; 2009; pp 204-207.

94. Al-Hazeem, N. Z.; Ahmed, N. M.; Mat Jafri, M. Z.; Ramizy, A., The effect of deposition angle on morphology and diameter of electrospun TiO2/PVP nanofibers. *Nanocomposites* **2021,** *7* (1), 70-78.

95. Yarin, A. L.; Kataphinan, W.; Reneker, D. H., Branching in electrospinning of nanofibers. *Journal of Applied Physics* **2005,** *98* (6), 064501.

96. Zhou, W.; He, J.; Cui, S.; Gao, W., Preparation of electrospun silk fibroin/Cellulose Acetate blend nanofibers and their applications to heavy metal ions adsorption. *Fibers and Polymers* **2011,** *12* (4), 431-437.

97. Jose Varghese, R.; Sakho, E. h. M.; Parani, S.; Thomas, S.; Oluwafemi, O. S.; Wu, J., Chapter 3 - Introduction to nanomaterials: synthesis and applications. In *Nanomaterials for Solar Cell Applications*, Thomas, S.; Sakho, E. H. M.; Kalarikkal, N.; Oluwafemi, S. O.; Wu, J., Eds. Elsevier: 2019; pp 75-95.

98. Pal, P.; Srivas, P. K.; Dadhich, P.; Das, B.; Maulik, D.; Dhara, S., Nano-/Microfibrous Cotton-Wool-Like 3D Scaffold with Core–Shell Architecture by Emulsion

Electrospinning for Skin Tissue Regeneration. *ACS Biomaterials Science & Engineering* **2017,** *3* (12), 3563-3575.

99. Suresh, S.; Gryshkov, O.; Glasmacher, B., Impact of setup orientation on blend electrospinning of poly-ε-caprolactone-gelatin scaffolds for vascular tissue engineering. *The International Journal of Artificial Organs* **2018,** *41* (11), 801-810.

100. Khatri, M.; Khatri, Z.; El-Ghazali, S.; Hussain, N.; Qureshi, U. A.; Kobayashi, S.; Ahmed, F.; Kim, I. S., Zein nanofibers via deep eutectic solvent electrospinning: tunable morphology with super hydrophilic properties. *Scientific Reports* **2020,** *10* (1), 15307.

101. Bhardwaj, N.; Kundu, S. C., Electrospinning: A fascinating fiber fabrication technique. *Biotechnology Advances* **2010,** *28* (3), 325-347.

102. Bealer, E. J.; Onissema-Karimu, S.; Rivera-Galletti, A.; Francis, M.; Wilkowski, J.; Salas-de la Cruz, D.; Hu, X., Protein–Polysaccharide Composite Materials: Fabrication and Applications. *Polymers* **2020,** *12* (2), 464.

103. Heinze, T.; El Seoud, O. A.; Koschella, A., *Cellulose Derivatives Synthesis, Structure, and Properties*. 1st ed. 2018. ed.; Springer International Publishing: Cham, 2018.

104. Fujimoto, T.; Takahashi, S.-i.; Tsuji, M.; Miyamoto, T.; Inagaki, H., Reaction of cellulose with formic acid and stability of cellulose formate. *Journal of Polymer Science Part C: Polymer Letters* **1986,** *24* (1), 495-501.

105. Zhang, Y.; Wang, J.; Liu, C.; Liu, Y.; Li, Y.; Wu, M.; Li, Z.; Li, B., Influence of drying methods on the structure and properties of cellulose formate and its application as a reducing agent. *International Journal of Biological Macromolecules* **2021,** *170*, 397-405.

106. Jin, C.; Xiang, N.; Zhu, X.; E, S.; Sheng, K.; Zhang, X., Selective 5-hydroxymethylfurfural production from cellulose formate in DMSO-H2O media. *Applied Catalysis B: Environmental* **2021,** *285*, 119799.

107. Heinze, T.; El Seoud, O. A.; Koschella, A., Cellulose Activation and Dissolution. In *Cellulose Derivatives: Synthesis, Structure, and Properties*, Springer International Publishing: Cham, 2018; pp 173-257.

108. Sutherland, T. D.; Young, J. H.; Weisman, S.; Hayashi, C. Y.; Merritt, D. J., Insect silk: one name, many materials. *Annu Rev Entomol* **2010,** *55*, 171-88.

109. Kundu, B.; Rajkhowa, R.; Kundu, S. C.; Wang, X., Silk fibroin biomaterials for tissue regenerations. *Adv Drug Deliv Rev* **2013,** *65* (4), 457-70.

110. Rudall, K. M.; Kenchington, W., Arthropod Silks: The Problem of Fibrous Proteins in Animal Tissues. *Annual Review of Entomology* **1971,** *16* (1), 73-96.

111. Valluzzi, R.; Winkler, S.; Wilson, D.; Kaplan, D., Silk: Molecular organization and control of assembly. *Philosophical transactions of the Royal Society of London. Series B, Biological sciences* **2002,** *357*, 165-7.

112. Elzoghby, A. O.; Elgohary, M. M.; Kamel, N. M., Implications of protein- and Peptide-based nanoparticles as potential vehicles for anticancer drugs. *Adv Protein Chem Struct Biol* **2015,** *98*, 169-221.

113. Stanton, J.; Xue, Y.; Waters, J. C.; Lewis, A.; Cowan, D.; Hu, X.; Salas-de la Cruz, D., Structure–property relationships of blended polysaccharide and protein biomaterials in ionic liquid. *Cellulose* **2017,** *24* (4), 1775-1789.

114. DeFrates, K.; Markiewicz, T.; Callaway, K.; Xue, Y.; Stanton, J.; Salas-de la Cruz, D.; Hu, X., Structure–property relationships of Thai silk–microcrystalline cellulose biocomposite materials fabricated from ionic liquid. *International Journal of Biological Macromolecules* **2017,** *104*, 919-928.

115. Lu, Q.; Zhang, B.; Li, M.; Zuo, B.; Kaplan, D. L.; Huang, Y.; Zhu, H., Degradation Mechanism and Control of Silk Fibroin. *Biomacromolecules* **2011,** *12* (4), 1080-1086.

116. Hu, X.; Kaplan, D.; Cebe, P., Effect of Water on Thermal Properties of Silk Fibroin. *Thermochimica Acta* **2007,** *461*, 137-144.